Deeply Virtual Compton Scattering (DVCS) with Jlab at 12 GeV

October 8, 2017

A Prospectus by

Bishnu Karki

Department of Physics and Astronomy
Ohio University

Committee Members:

Dr. Julie Roche (Advisor)
Dr. Daniel Phillips
Dr. Katherine Cimatu
Dr. Kenneth H. Hicks

Abstract

Data taking for the experiment E12-06-114 (DVCS) was completed at the end of 2016. This experiment ran in Hall A in Jefferson Lab (JLab). We used the polarized electron beam ranging from 8 to 11 GeV to measure the polarized and unpolarized cross-section of H(e,e'γ)p to extract the Generalized Parton Distributions (GPDs) of the proton. The wide range of Q^2 scans ($2 < Q^2 < 9\ GeV^2$) was performed at three different values of the Bjorken variable (x_B) from 0.36 to 0.60 to validate the GPDs formalism in the regime accessible at Jlab. The scattered electron was measured by the high-resolution spectrometer in Hall A, the final photon was measured by the DVCS dedicated calorimeter and the recoiled proton is reconstructed using the missing mass technique. In this proposal, I will present my involvement with DVCS collaboration and status of an experiment to this point. At the end, I will discuss my future plans for graduation by Spring 2019.

Contents

1 Introduction

The Proton and neutron (collectively known as nucleons) are the building blocks of atomic nuclei, which forms most of the visible matter around us. Nucleons interact with each other via strong interaction and this strong interaction determines the properties of atomic nuclei. The strong interaction governs the nuclear reactions that shaped the early universe, fuel the stars and those in the nuclear reactors. Deep Inelastic Scattering (DIS) showed that nucleons are composite objects made up of fundamental particles called quarks. The strong force between the quarks binds them to form nucleons. The strong force is unique, it does not obey the inverse-square law. Moreover, the mediating particles for the strong force, called gluons, interact among themselves. The modern theory of the strong interaction is Quantum Chromodynamics (QCD), a field theory, whose fundamental degrees of freedom are quarks and gluons. The coupling constant for the strong force (α_s) depends on the distance scale (energy of probe). Based on this fact, QCD is usually divided into two regions:

a) Asymptotic freedom: At short distances (momentum transferred $>$ few GeV^2), α_s is small and the quarks behave as if they are free. Perturbation theory can be used to make calculations.

b) Confinement: At larger distance scales comparable to a dimension of a nucleon, α_s will be near unity. A quark strongly interacts with other neighboring quarks, so a quark cannot be isolated from nucleons. Instead, they remain confined within a nucleon. In this regime, perturbative calculations are not valid.

The strong interaction is not fully understood, especially in the confinement regime. Understanding how quarks and gluons interact with each other to form a nucleon is one of the key objectives of nuclear physics. Experimentally we can study the structure of a nucleon using an electron beam as a probe. The experimental results help us to understand the transition from asymptotic freedom to the confinement regime, thus improving our understanding of the strong force.

We have information about the structure of the nucleon from scattering experiments. The electromagnetic Form Factors (FFs) measured in elastic scattering of electrons off protons give the spatial distribution of quarks in the transverse plane. However, the information about the momentum distribution about quarks gets washed out. On the other hand, the Parton Distribution Functions (PDFs) measured in the Deep Inelastic Scattering (DIS) of electrons off protons give the momentum distribution of the quarks, but the information about the spatial distribution gets integrated out. Both FFs and PDFs give a one-dimensional description of the internal structure of the nucleon. There was a need for functions which could relate FFs and PDFs and contain some higher level of information on nucleon structure. Later, in mid 90's the concept of new functions called Generalized Parton Distributions (GPDs) [1–3] was introduced it took the description of the internal structure of nucleon to a new level. GPDs encapsulate the correlation between the spatial distribution and momentum distribution of quarks inside the nucleons. As the consequence, GPDs give access to the orbital angular momentum of quarks [1] which has not been measured so far. Thus, GPDs help us to understand the complete spin structure of nucleons.

The factorization theorem proved that the scattering of electrons off the protons can be factorized into two parts: A hard/perturbative part and a soft/non-perturbative part. As a

result of factorization, the measured scattering cross section can be parametrized by some functions associated with the soft part. These functions associated with soft part give insight into a nucleon structure. The soft part of deep exclusive processes, where all the final products are measured, can be parametrized by GPDs. Due to advancements in technology (high luminosity beam, good resolution detectors, etc.), we can get access to GPDs experimentally via deep exclusive processes like Deeply Virtual Compton Scattering (DVCS) or Deeply Virtual Meson Production (DVMP) [1]. Unlike DVMP, DVCS has only one non-perturbative object (two in DVMP one additional from meson production) which makes DVCS as one of the cleanest ways to measure the GPDs.

So far several attempts have been made to extract the experimental observables related to GPDs. To have a complete picture of nucleon structure one needs to measure the different observables at a wide range of kinematics. At the end, we can reconcile our knowledge from different observables at a different kinematic range and have the robust model independent way of describing the nucleon structure. However, due to the design of experimental facilities, one cannot measure all observable in a broad kinematic range in a single facility by a single group. Nevertheless, different collaborations have used different available beam facilities around the world to measure the DVCS observables at the different kinematic regime. Collaborations such as H1 and ZEUS measured the DVCS cross section by colliding proton beam from HERA, at DESY, with the positron beam at low Bjorken variable (x_B). These collaborations took advantage of high-energy available from the collision and went to high Q^2 (squared of four-momentum transfer). They also studied the dependence of the DVCS cross section on different kinematic variables [4]. Other collaborations like the HERMES [5] and CLAS [6] measured the various beam and target asymmetries at higher x_B (valence regime). Unlike the H1 and ZEUS, they were fixed target experiments at low Q^2. Earlier in 2002 and 2010, the DVCS experiments collected data in Hall A in JLab. The results from these experiments are already published. First experiment [7] illustrated the feasibility of the experiment and also proved the reliability of our experimental method. However, this measurement was limited in kinematic coverage due to the maximum available beam energy (Max. 6 GeV).

We have learned a lot from these pieces of information we got from different measurements. But now we are in the phase of precision measurement. The experiment E12-06-114 adapts well-established methods verified by first two generations of experiments in Hall A to measure the absolute cross section of the DVCS process with high precision (5% relative precision) [8] in valence regime. For the given Bjorken variable (x_B), we have several Q^2 scans to validate the GPDs formalism. The DVCS experiment (E12-06-114) is one of the first experiment after the CEBAF was upgraded to 12 GeV. It uses the polarized electron beam from Continuous Electron Beam Accelerator Facility (CEBAF). The polarized electron scatters through the liquid hydrogen target in a deep inelastic regime. All the final products scattered electron, final real photon, and recoiled proton are identified. Scattered electron is detected on High Resolution Spectrometer (HRS), a photon is detected in DVCS dedicated Lead Fluoride calorimeter, and the recoiled proton is reconstructed using the missing mass technique (energy and momentum conservation). Experiment E12-06-114 is the subject of this document and part of my proposed thesis work. In this document, I will present my contribution to experiment E12-06-114, the status of the experiment, and my future plans for graduation.

2 Generalized Parton Distributions

In the 1960s, Friedman and his team confirmed that a proton is a composite object made of partons (quarks and gluons). Since then physicists have put a lot of effort in understanding how quarks build up the proton. Basically, there are two approaches to study nucleon, a collective name for proton and neutron, structure: The first one is an elastic scattering of electron off proton in which nucleon structure is parametrized by the Form Factors (FFs). The Fourier transform of FFs gives the spatial distribution of the internal constituents of a nucleon. However, FFs do not provide any information about the dynamics of the quarks. Deep Inelastic Scattering (DIS) is the other way of studying the internal structure of a nucleon. The cross section of this process can be parametrized by the Parton Distribution Functions (PDFs) functions. These PDFs gives access to longitudinal momentum distribution of quarks inside the nucleons, but do not contain any information on spatial distribution of quarks. Unfortunately, neither FFs nor PDFs provide the complete information about the interior of a nucleon.

Later in the mid 90's, Generalized Parton Distributions (GPDs) [1–3] were introduced as a novel technique to describe the internal structure of the nucleon. GPDs are recognized as powerful tools to investigate the internal structure of nucleon because they parametrize the correlation between longitudinal momentum and spatial distribution of quarks. Hence, GPDs encode higher level of information about the interior picture of a nucleon. Experimentally, GPDs are accessible via deep exclusive processes where all the final products are detected. The factorization theorem [9] proved that the GPDs can be accessed from deep exclusive processes. In this document, we will focus on DVCS to access GPDs. Figure 1 is the handbag diagram for the DVCS process ($\gamma^* p \to \gamma p$) at leading twist, where the incoming electron interacts with a single quark via a virtual photon. The struck quarks is re-absorbed by the proton emitting the real the photon. The different kinematic variables for DVCS process are defined in Table 1. At the Broken limit;

$$\left.\begin{array}{l} Q^2 \to \infty \\ \upsilon \to \infty \end{array}\right\} \quad \text{at fixed } x_B \tag{1}$$

the handbag amplitude in Figure 1, at leading twist and leading order, can be factorized into two parts as shown by the dashed line. The hard scattering part (shown above the dashed line) is exactly calculable by using pQCD, while the soft part (shown below the dashed line) is a non-perturbative object and can not be calculated using Quantum Chromodynamics (QCD). The soft part encodes the information about nucleon structure and is parametrized by 4 quark GPDs. GPDs are functions of the three variables x, ξ , and t. The parameter x is the average longitudinal momentum fraction carried by the struck quark, ξ and t are defined in Table 1. x and ξ parametrize the longitudinal momentum fraction of parton while t contains the information about the spatial distribution of quarks in the transverse plane. H(x,ξ,t) and E(x,ξ,t) are beam helicity independent GPDs while $\widetilde{H}$(x,ξ,t) and $\widetilde{E}$(x,ξ,t) are beam helicity dependent GPDs. On other hand, H(x,ξ,t) and $\widetilde{H}$(x,ξ,t) are nucleon helicity conserving GPDs while E(x,ξ,t) and $\widetilde{E}$(x,ξ,t) allow the possibility of the nucleon helicity flip.

2.1 Properties of GPDs

Scattering of virtual photon on a single parton is leading contribution to DVCS at high Q^2 and is termed as leading twist contribution. The simultaneous scattering of virtual photon on

Variables	**Definition**	**Expression**
E	Energy of incoming e^- beam	-
E'	Energy of outgoing e^-	-
M	Mass of proton	-
k	4-momentum of incoming e^- beam	-
k'	4-momentum of outgoing e^-	-
p	4-momentum of target proton	-
p'	4-momentum of recoiled proton	-
Q^2	Squared of 4-momentum transfer (resolution of probe)	Q^2 = $-q^2 = (k - k')^2$
υ	Energy loss or transferred by electron	υ= E - E'
x_B	Bjorken variable	$x_B = \frac{Q^2}{2M\upsilon}$
t	Squared of 4-momentum transfer to proton	t = $-\Delta^2 = (p' - p)^2$
y	e^-'s fractional energy loss	y=$\frac{\upsilon}{E}$
W^2	Invariant mass of final hadronic state	$W^2 = M^2 + Q^2 \left(\frac{1}{x_B} - 1\right)$
ξ	Longitudinal fraction of momentum transfer to the nucleon	$\xi = \frac{x_B}{2-x_B}$

Table 1: *Definition of kinematics variable for DVCS process.*

two or more partons is the higher twist contribution and is suppressed at high Q^2. At leading twist, the GPDs depend on the three variables: x, ξ, and t. The variables ξ and t can be accessed by measuring the kinematics of the scattered electron and the final state photon or proton, but the variable x is not experimentally accessible. In the calculation of the DVCS amplitude of handbag diagram in Figure 1, the variable x is integrated over. Therefore, GPDs are not directly accessible from the experiment. Instead, we measure Compton Form Factors (CFFs) [11]. GPDs enter the DVCS cross section through CFFs which are the function of ξ and t. Equation 2 shows the connection between the CFF, $\mathcal{H}(\xi$,t) and the GPD H(x,ξ,t) for flavour f ϵ {u,d,s}

$$\mathcal{H}(\xi,t) = \sum_f \frac{e_f^2}{e^2}\left\{ i\pi[H_f(\xi,\xi,t) - H_f(-\xi,\xi,t)] + \mathcal{P}\int_{-1}^{1} dx \left[\frac{1}{\xi - x} - \frac{1}{\xi + x}\right] H_f(x,\xi,t)\right\} \quad (2)$$

GPDs are generalized forms of PDFs and FFs in other word PDFs and FFs are the limiting case of GPDs. In the limit, t $\to$ 0 and $\xi \to 0$ GPDs reduce to partonic distribution as:

$$\begin{aligned} H^f(x,0,0) &= q_f(x) \\ \widetilde{H}(x,0,0) &= \Delta q_f(x) \end{aligned} \quad (3)$$

where f is a flavour of quark and $q_f(x)$ and $\Delta q_f(x)$ are unpolarized and polarized quark densities.

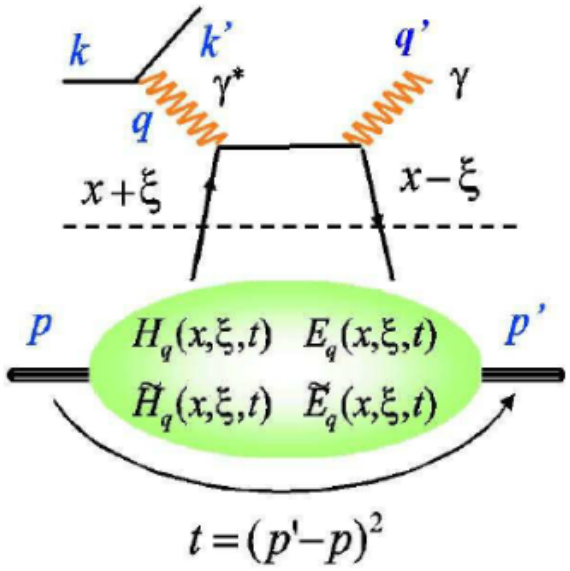

Figure 1: *Handbag diagram for DVCS process at leading twist and leading order. The incoming electron interacts with a single quark via virtual photon and a real photon is emitted from the proton. In the Bjorken limit, this interaction can be factorized in two parts: the hard part which is exactly calculable using QED and the soft part (non-perturbative) part that encodes the nucleon structure and can be parametrized by GPDs. This figure was taken from [10].*

The first moments of GPDs are related to the elastic form factors [12] as :

$$\begin{aligned}
\int_{-1}^{1} H^f(x,\xi,t)dx &= F_1^f(t) \\
\int_{-1}^{1} E^f(x,\xi,t)dx &= F_2^f(t) \\
\int_{-1}^{1} \widetilde{H}(x,\xi,t)dx &= G_A^f(t) \\
\int_{-1}^{1} \widetilde{E}(x,\xi,t)dx &= G_p^f(t)
\end{aligned} \tag{4}$$

where $F_1^f(t)$, $F_2^f(t)$, $G_A^f(t)$ and $G_p^f(t)$ are Dirac, Pauli, axial and pseudo-scalar form factors respectively. As PDFs and FFs are known well so the above connections between GPDs and FFs/PDFs are crucial to test the measured GPDs.

To understand QCD one need to understand the spin structure of the proton. The total spin of the proton can be written as the sum of spin from constituent quarks and spin from gluons:

$$\frac{1}{2} = \underbrace{\frac{1}{2}\Delta\Sigma + L_q}_{J^q} + J_g$$

where J_q and J_g are the total angular momentum of quarks and gluons while L_q orbital angular momentum of quarks and $\frac{1}{2}\Delta\Sigma$ is the sum of spin from quarks. Measurements show the spin

contribution from quarks and gluons do not add up to the total spin of the proton. Thereby, leaves the

essence of measuring the contribution from the orbital angular momentum of quarks which has not been measured so far. GPDs can give access to the orbital angular momentum of quarks via Ji's sum rule [1].The total angular momentum of quarks J^q can be accessed from the GPDs as:

$$J^q = \int_{-1}^{1} x[H^f(x,\xi,0) + E^f(x,\xi,0)]dx \tag{5}$$

This property makes GPDs more exciting in physicist community.

2.2 GPDs via DVCS

Photo-electroproduction (ep $\rightarrow$ $ep\gamma$) has a contribution from processes with the similar outcomes called DVCS and Bethe-Heitler (BH), they are experimentally indistinguishable. Figure 2a shows the DVCS process where the photon is radiated from the proton. At a leading order and a leading twist, DVCS process is described by handbag diagram shown in Figure 1. Figures 2 b and c show the BH process where the photon is either radiated from an incoming or outgoing electron. In the BH process, the nucleon structure is encoded by FFs. Since the DVCS ampli-

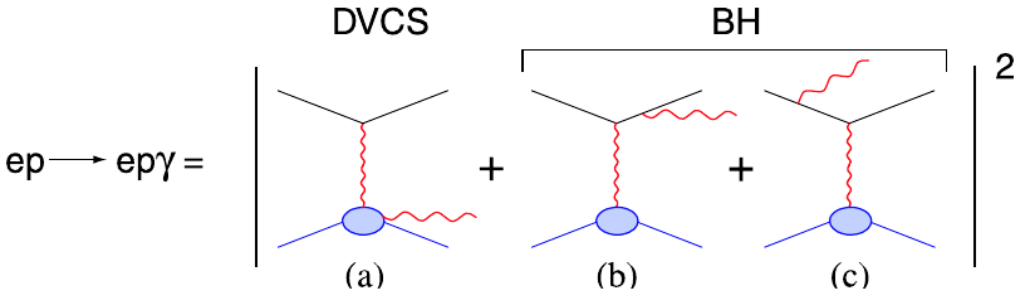

Figure 2: *Contribution to the ep $\rightarrow$ epγ from DVCS and BH processes. In DVCS (a), the photon is radiated from proton while in BH (b and c) the photon is either radiated from incoming or outgoing electron.*

tude interferes with the BH, the 5-fold differential cross section for photon electroproduction can be written as [13]:

$$\frac{d^5\sigma}{dQ^2 dt dx_B d\phi_e d\phi} = \frac{\alpha^3 x_B y}{16\pi^2 Q^2 \sqrt{1+4x_B^2 M^2/Q^2}} \mid \frac{\mathcal{T}}{e^3} \mid^2 \tag{6}$$

where the kinematic variable $\epsilon = \frac{2x_B M}{Q}$. Angle ϕ_e is electron azimuthal angle with respect to the horizontal plane around the beam line direction, ϕ is the azimuthal angle between leptonic and hadronic plane. Figure 3 shows the definition of angle ϕ as by Trento Convention [14] . The total amplitude ($\mathcal{T}$) is the sum of DVCS ($\mathcal{T}_{DVCS}$) amplitude, BH amplitude ($\mathcal{T}_{BH}$), and the interference between these two process ($\mathcal{I}$).

$$\begin{aligned} \mid \mathcal{T} \mid^2 &= \mid \mathcal{T}_{DVCS} \mid^2 + \mid \mathcal{T}_{BH} \mid^2 + \mathcal{I} \\ \mathcal{I} &= \mathcal{T}^{\dagger}_{DVCS}\mathcal{T}_{BH} + \mathcal{T}^{\dagger}_{BH}\mathcal{T}_{DVCS} \end{aligned} \tag{7}$$

The harmonic expansions of term $\mathcal{T}_{DVCS}$, $\mathcal{T}_{BH}$ and $\mathcal{I}$ up to twist 3 , in term of angle ϕ, can be expressed as:

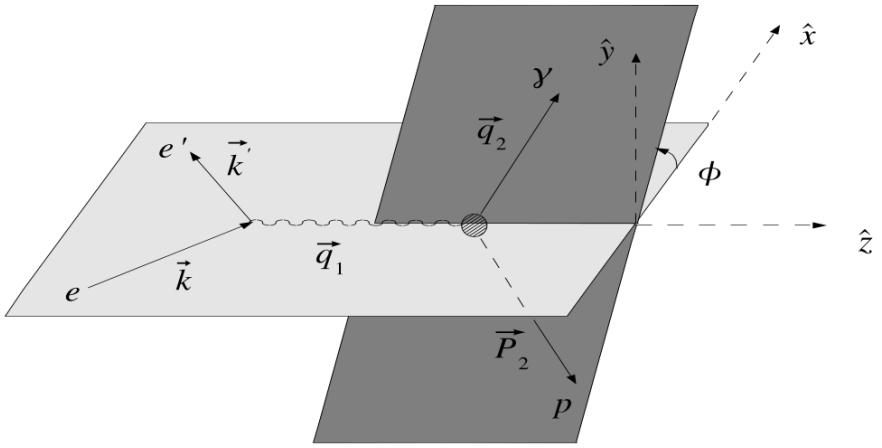

Figure 3: *Kinematics for photo electroproduction in target rest frame. The azimuthal angle ϕ is an angle between the electron scattering plane and the hadronic production plane. This figure is adapted from [15].*

$$| \mathcal{T}_{BH} |^2 = \frac{e^6}{x_B^2 y^2 (1+\epsilon^2)^2 \Delta^2 \mathcal{P}_1(\phi)\mathcal{P}_2(\phi)} \left\{ \mathcal{C}_0^{BH} + \sum_{n=1}^{2} \mathcal{C}_n^{BH} cos(n\phi) + \mathcal{S}_1^{BH} sin(\phi) \right\} \tag{8}$$

$$| \mathcal{T}_{DVCS} |^2 = \frac{e^6}{y^2 Q^2} \left\{ \mathcal{C}_0^{DVCS} + \sum_{n=1}^{2} \left[\mathcal{C}_n^{DVCS} cos(n\phi) + \mathcal{S}_n^{DVCS} sin(n\phi) \right] \right\} \tag{9}$$

$$\mathcal{I} = \frac{\pm e^6}{x_B y^3 \Delta^2 \mathcal{P}_1(\phi)\mathcal{P}_2(\phi)} \left\{ \mathcal{C}_0^{I} + \sum_{n=1}^{3} \left[\mathcal{C}_n^{I} cos(n\phi) + \mathcal{S}_n^{\mathcal{I}} sin(n\phi) \right] \right\} \tag{10}$$

$$\begin{aligned}
\mathcal{P}_1(\phi) &= -\frac{J + 2K cos(\phi)}{y(1+\epsilon^2)}, \\
\mathcal{P}_2(\phi) &= 1 + \frac{t}{Q^2} + \frac{J + 2K cos(\phi)}{y(1+\epsilon^2)}, \\
J &= \left(1 - y - \frac{y\epsilon^2}{2}\right)\left(1 + \frac{t}{Q^2}\right) - (1 - x_B)(2 - y)\frac{t}{Q^2}, \\
K^2 &= -\frac{\Delta^2}{Q^2}(1 - x_B)\left(1 - y - \frac{y^2\epsilon^2}{4}\right)\left(1 - \frac{\Delta^2_{min}}{\Delta^2}\right)\left(\sqrt{1+\epsilon^2} + \frac{4x_B(1-x_B) + \epsilon^2\Delta^2 - \Delta^2_{min}}{4(1-x_B)}\right), \\
-\Delta^2_{min} &\approx \frac{M^2 x_B^2}{1 - x_B + x_B M^2/Q^2}
\end{aligned} \tag{11}$$

The harmonics coefficients of the interference term are linear combination of Compton Form Factors (CFFs) [16]. The terms in DVCS amplitude, $\mathcal{C}_i^{DVCS}$ and $\mathcal{S}_i^{DVCS}$, can be expressed as a bilinear combination of CFFs. The coefficients $\mathcal{C}_i^{BH}$ and $\mathcal{S}_i^{BH}$ depend on the electromagnetic form factors of a nucleon. Furthermore, the coefficients C_1^I, S_1^I and C_0^{DVCS} arise at the twist-two level. Rest coefficients C_1^{DVCS}, S_1^{DVCS}, C_2^I and S_2^I are given in terms of twist-three GPDs [13].

To have the complete information of internal structure of nucleon one need to measure 8 different CFFs. Different observables like polarized/unpolarized cross-section, various asymmetries (beam charge asymmetry, beam spin asymmetry, target spin asymmetry) are sensitive to combination of different CFFs. To disentangle the full sets of CFFs one need to measure several observables in wide kinematic range. For instance, the σ_{unp} cross section is sensitive to the real part of the DVCS amplitude while the σ_{pol} is sensitive to the imaginary part of DVCS amplitude.

$$\begin{aligned} \sigma_{pol} &= \overrightarrow{\sigma} - \overleftarrow{\sigma} = 2 \cdot \mathcal{T}_{BH} \mathcal{I}m \cdot \mathcal{T}_{DVCS} \\ \sigma_{unp} &= \overrightarrow{\sigma} + \overleftarrow{\sigma} = \mid \mathcal{T}_{BH} \mid^2 + 2 \cdot \mathcal{T}_{BH} \mathcal{R}e \cdot \mathcal{T}_{DVCS} \end{aligned} \tag{12}$$

2.3 DVCS Experiments:

Over the last two decades, lots of effort has been made to measure the DVCS observables in different kinematic regimes. Figure 4 shows worldwide DVCS programs. These programs have proved the feasibility of GPDs measurement and also have provided some insights on nucleon structure. H1 and ZEUS collaborations measured the DVCS cross section at high energy (30 $<$ W $<$ 140 GeV) , Fwith Q^2 range, $2 < Q^2 < 100\ GeV^2$. They used 820 GeV proton beam from HERA to collide with electron/positrons with energy 27.5 GeV. They measured the DVCS cross section dependence on different kinematic variables like Q^2, W^2, and t. Furthermore, the contribution from the real part of the DVCS amplitude was observed for the first time in a collider mode[17, 18].

The helicity asymmetry in DVCS has been measured at lower energy with polarized lepton beams by HERMES [5] at DESY and CLAS [6] at Jlab. HERMES measurements were at Q^2 ranging from 1 to $\sim$6 GeV^2 and x_B from 0.04 to 0.2. They took advantage of both electron and positron polarized beam and measured the complete set of asymmetries to unfold the different CFFs contribution. CLAS collaboration studied the beam spin asymmetries using the longitudinally polarized electron beam with liquid hydrogen target and double spin asymmetries with longitudinally polarized NH_3 target. They also measured the unpolarized and polarized cross section at beam energy 5.75 GeV [19]. CLAS collaboration took advantage of their large acceptance spectrometer and covers a wide kinematic range. However, their measurement has high uncertainty ($\sim$15%) in some of the kinematic bins.

In Hall A, two generations of DVCS dedicated experiments have already been done using beam 6 GeV beam energy. These are high luminosity and high precision experiments which demonstrated the sensitivity of this data to the higher-twist or next to leading order which are usually neglected in recent phenomenology [20]. This measurement was limited in Q^2 from 1.5 to $\sim$2 GeV^2 and at single x_B, 0.36. Figure 5 shows the contribution from different terms in polarized and unpolarized cross section. The unpolarized cross section has a significant contribution from $\mid \mathcal{T}_{DVCS} \mid^2$ along with the interference term. The polarized cross section is dominated by twist-2 interference term. The DVCS3, third generation experiment at Hall A (the topic of my research), adopts the well-established methods used in the first two generations at

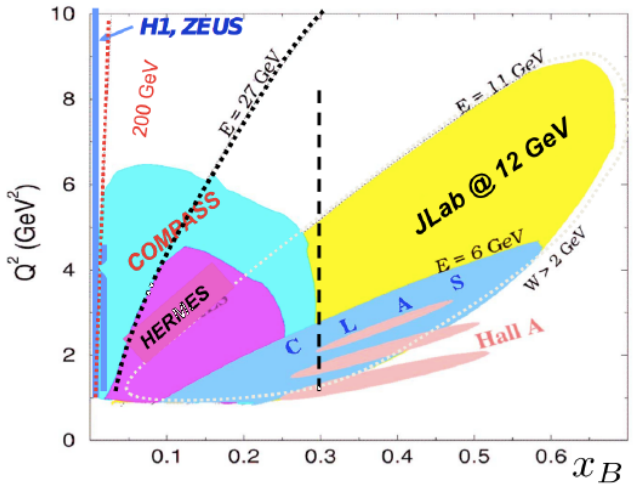

Figure 4: *DVCS measurement in Q^2 and x_B phase space covered by different collaborations.*

6 GeV. It uses the longitudinally polarized electron beam from CEBAF (Continuous Electron Beam Accelerator Facility), and liquid hydrogen target to measures high precision absolute DVCS cross section taking advantage of the high beam energy available with CEBAF at 12 GeV.

Beside all these facilities, COMPASS at CERN also has the GPDs program with muon beam at low x_B and high Q^2. In addition to that, Electron-Ion Collider (EIC) also has compelling GPDs programs in future [21].

2.4 Extraction of GPDs from data

As discussed earlier, GPDs cannot be directly accessed through experiments due to the presence of closed loop in DVCS process. Instead, they are extracted by fitting the experimental observables similar to PDFs. But the extraction of GPDs from the data is relatively complicated as GPDs are function of there different variable x, ξ, and t . However, fits to the DVCS data has been successfully performed and GPD phenomenology has turned into a matured field. The brief description of some of the fitting methods are described below:

2.4.1 Global fits of GPDs

Global fit requires physically motivated parametrization of GPDs. For each experimental data sets, all kinematic bins at once in global fit. Its main advantage is the ability to extrapolate outside of the data region. Global fits have been used to extract the GPDs H_{Im} and $\widetilde{H}_{Im}$ from the existing data [11].

2.4.2 Local fits of CFFs

It assumes the fact that several observables can be measured at a single kinematical point. Local fits takes each kinematic bin independently of the others. As a intermediate step, the

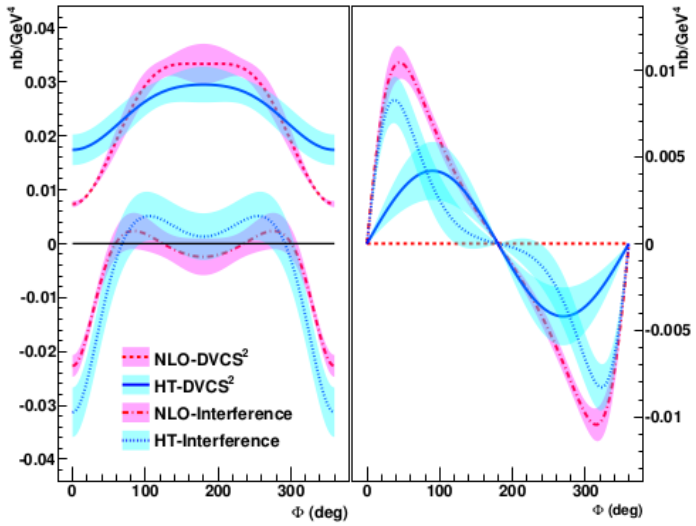

Figure 5: *A generalized Rosenbluth separation of the total electroproduction of a photon. The shown data is at Q^2 =1.75 GeV^2 , x_B = 0.36 and t = -0.32 GeV^2 for helicity dependent cross section (right and helicity-independent cross section (left). A $DVCS^2$ contribution appears in the helicity dependent cross section only if there is a contribution from the longitudinal polarization of the virtual photon. This figure is adapted from [20].*

CFFs are extracted as numbers for fixed ξ and t rather than extracting function CFF(ξ,t) [22]. So the local fits are free of the serious model biases (at leading-twist). But in this method, CFFs are fitted instead of GPDs. Nevertheless, local fits can provide quite direct information about the structure function in given kinematic range.

Figure 6 shows the example of local and global fitting of polarized and unpolarized DVCS cross section measured at Hall A [23]. It also shows the comparison with VGG model prediction. N_{max} represents the truncation in Gegenbauer polynomial expansion [24] which is used for global fitting. N_{max} = 2, 3, and 4 corresponds to 10, 18 and 28 fitting parameters respectively. Global and local fits to helicity-dependent and helicity-independent cross section are all good, and almost indistinguishable with N_{max}=3. Along with these two fitting methods others methods like Hybrid fits of GPDs and neural network fits of GPDs are also used to extract the GPDs from the data [11].

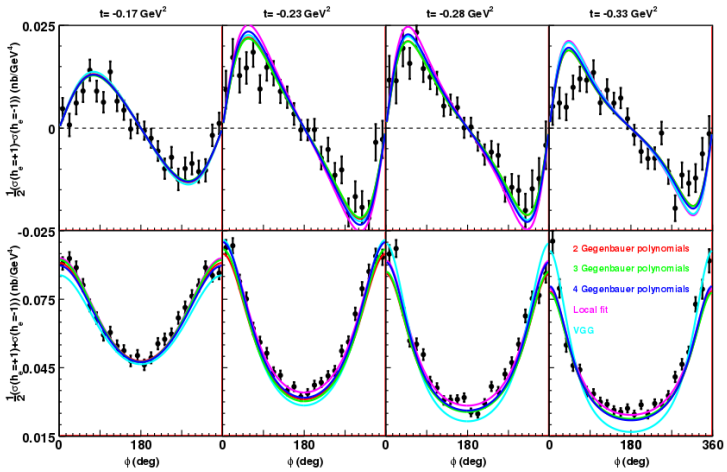

Figure 6: *Fits for helicity dependent (up) and helicity independent cross section measured at Jefferson Lab Hall A. The results with global fits (N_{max} 2, 3, and 4), local fits and prediction from VGG model. This figure is adapted from [23]. The results for local and global fits are almost always compatible.*

3 The E12-06-114 Experiment

The first DVCS experiment in Hall A, E00-110, measured both polarized and unpolarized DVCS cross sections for different Q^2 ranging from 1.5 to 2.3 GeV^2 at a fixed x_B of 0.36. However, this experiment (E00-110) was limited by the kinematic coverage in x_B and Q^2. Nevertheless, result from E00-110 showed that the GPDs can be accessible at the moderate Q^2 available at JLab. In addition, it also illustrated the reliability of our methodology and motivated for the new experiment which can cover the broader phase space. Experiment, E12-06-114, covers wide phase space in Q^2 ($2 < Q^2 < 9\ GeV^2$) and x_B (0.3 to 0.6) accessible by 11 GeV in Hall A. The main goals of this experiment E12-06-114 are [8]:

- To measure both helicity-dependent and helicity-independent cross sections of the $ep \to e'p'\gamma$ at fixed x_B over a wide range of Q^2, accessible with 11 GeV at Jefferson Lab, with high precision (∼5% relative precision). This will help us to prove that the GPD formalism is appropriate to describe the nucleon structure in this regime.

- To measure $ep \to e'p'\pi^0$ cross section. From pion electroproduction data one can estimated the handbag contribution to longitudinal cross section σ_L which is only leading twist term in electroproduction cross section. Moreover, the Fourier decomposition of azimuthal dependence of the cross section allows one to obtain the interference (longitudinal and transverse virtual photon polarization) terms: σ_{LT}, σ_{TT}, $\sigma_{LT'}$. These observables will provide additional constraints on both the longitudinal and transverse currents in pion electroproduction. will test the factorization dominance of meson electroproduction.

3.1 Status of Experiment

Experiment E12-06-114 ran in Jefferson lab at Hall A from the Fall of 2014 to the Fall of 2016. It is one of the first experiment after 12 GeV upgrade so there were a lot of issues in the accelerator. We were approved for 50 PAC days of data taking i.e running 50 days with 100% accelerator efficiency. But we took data for about 124 calendar days (because of a relatively lower efficiency of accelerator). Due to the reduced efficiency of the accelerator, we collected less statistics in some of our kinematics and even missed some of our proposed kinematic points at x_B of 0.60. Table 2 shows different kinematic variables for the runs taken at different periods of time. In each kinematic data is taken for several days depending on the rate. In order to store the data in sizable files (4 GB) data taking process is chopped into many segments each of approximately an hour of data. Each of this segment/file with an hour of data is termed as a run. Figure 7 shows the "VGG" GPD model [25] prediction of the structure function, Imaginary part of $\mathcal{C}_0^I$ in Equation 9, as a function of Q^2. The Q^2 independence of the structure function is termed as scaling behavior which validates the GPDs formalism to describe the nucleon structure. The error bar on the data point predicated by "VGG" model is much smaller which is one of the exciting part of this experiment. The different color code represents the different period of data taking. We missed two of the proposed data points at x_B=0.60 due to the time limitation.

Period	Kinematics	Beam Energy (GeV)	Q^2 (GeV^2)	x_B
Fall 2014	Kin36-1	6.66	3.2	0.36
Fall 2016	Kin36-2	8.52	3.6	0.36
Fall 2016	Kin36-3	10.62	4.47	0.36
Spring 2016	Kin48-1	4.48	2.7	0.48
Spring 2016	Kin48-2	8.84	4.37	0.48
Spring 2016	Kin48-3	8.84	5.33	0.48
Spring 2016	Kin48-4	11.02	6.90	0.48
Fall 2016	Kin60-1	8.52	5.54	0.60
Fall 2016	Kin60-3	10.62	8.4	0.60

Table 2: *Actual kinematics covered by E12-06-114 experiment. We started taking data from Fall 2014 and completed our data taking at the end of 2016. The data cover wide range in Q^2 ($2 < Q^2$ 9 GeV^2) for different values of x_B.*

3.2 Methodology

This experiment was conducted in Hall A in Jefferson Lab. Longitudinally polarized electron beam from CEBAF ranging from 8 to 11 GeV is fired on fixed proton target (liquid hydrogen). The scattered electrons are detected in Left High Resolution Spectrometer (LHRS) which will be discussed in later section 4.1.3. The final photon is detected in DVCS dedicated calorimeter which will be also discussed later. Figure 8 shows the experimental setup for this experiment. The recoiled proton is not directly measured. Instead, it is reconstructed using the energy and momentum information of incident electron, target proton, scattered electron, and final photon (missing mass technique). The invariant mass of missed hadron in the final state is given as:

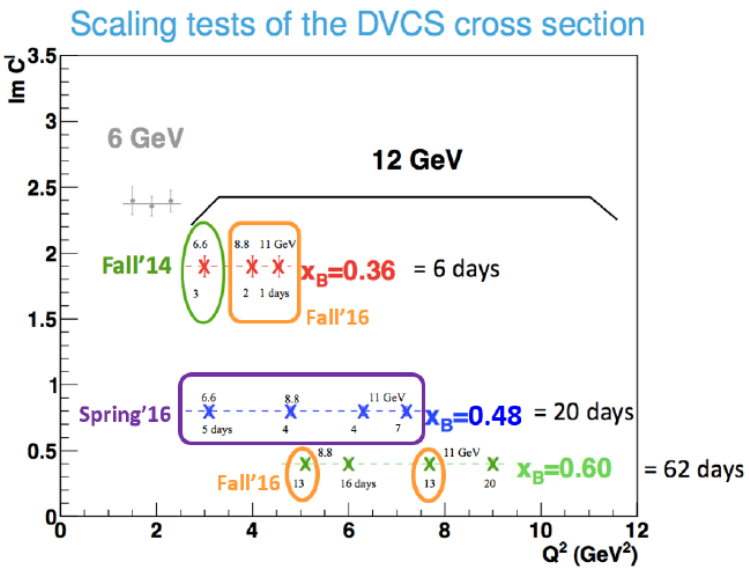

Figure 7: *The Q^2 and x_B phase space covered by E12-06-114 experiment. Each color represents the different period of data taking. Some of this purposed kinematics were not covered during this run period. Data points are the VGG model [25] prediction of the structure function ($\mathcal{C}_0^I$). $\mathcal{C}_0^I$ is independent of Q^2 validates the GPD formalism.*

$$M^2_{ep->e'\gamma X} = (k + p - k' - q)^2 \tag{13}$$

where k, p, k', q are the four momentum vectors of the incident e^-, the target proton, scattered e^-, and the real photon respectively. The exclusivity of the DVCS process, H(e,e'γ)p, is ensured by applying the cut on background subtracted missing mass squared distribution. The resolution in missing mass of hadron is dominated by resolution of the calorimeter. The typical missing mass squared distribution of final missed hadron is shown in Figure 9 to select the DVCS events. The tail of the missing mass distribution is due to the radiative corrections and energy leak from the calorimeter.

3.3 Source of Background

The main sources of background are:

- π^0 productions (ep$\rightarrow e'p'\pi^0$): About 99% of the time π^0 decays into two photons, this π^0 decay may be symmetrical or asymmetrical. In symmetrical decay, both the photons carry the equivalent energy and both can be detected in the calorimeter (unless π^0 is directed to the edge of the calorimeter). We can reconstruct the pion mass from the invariant masses of these two photons and thus can be separated from DVCS events. In asymmetrical decay, one photon will be more energetic than the other. Because of the calorimeter software threshold ($\sim$ 1 GeV) we can detect only one (energetic) photon while the less energetic one can be missed out. If the energy of a detected photon is compatible with the DVCS photon then using the missing mass technique one cannot distinguish between the π^0 production and DVCS event. However, this contamination resulting from π^0

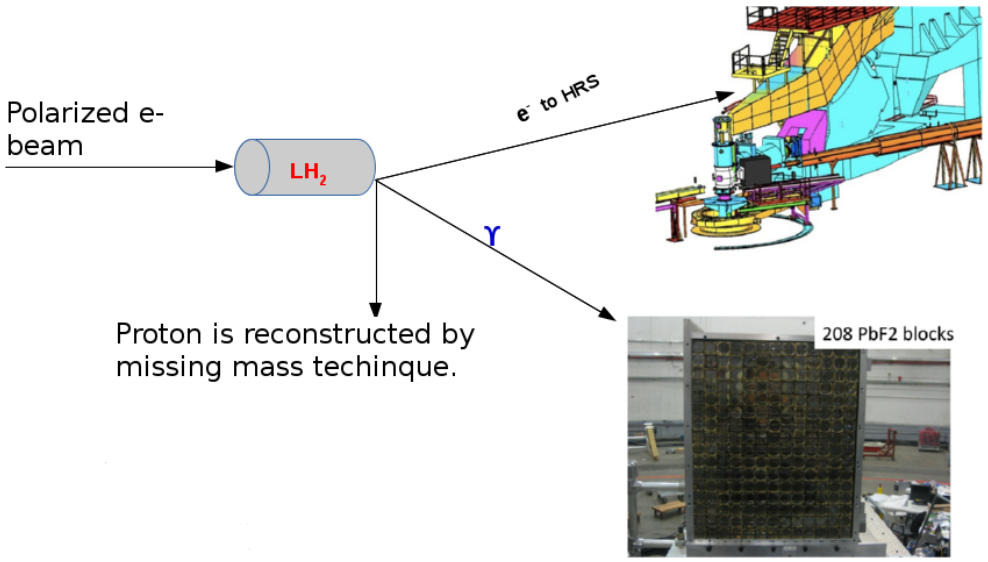

Figure 8: *Experimental setup for E12-06-114 in Hall A at Jefferson Lab. Polarized e^- scatters of the liquid hydrogen target (unpolarized). The scattered e^- and final γ are detected in Left HRS and DVCS calorimeter respectively.*

production can be corrected by extrapolating the number of π^0 symmetric decay detected in calorimeter using the Monte-Carlo simulation. The main advantage of this method is that we can have the number of π^0 symmetric decays directly from the experiment without having to rely on outside prediction.

- Accidental events: Some times we may have the photon in the calorimeter and electron in HRS within the coincidence time window but they might not be necessarily correlated (from different events). These events are called accidental events and should be subtracted from the signal. For accidental events correction, we take the events which have HRS and calorimeter in coincidence. Based on the fact that the probability of the accidental event is independent of time we can estimate the contribution from accidentals events. For example, Figure 10 shows the time spectrum of the coincidence events. The red filled section of the histogram shows the events within our coincidence window (accidentals + DVCS). Rest events are due to the accidental coincidences. We expect the same number of accidental events in our coincidence window (red) as in any other time window. To minimize the statistical uncertainty, we take the average of accidental events in two different time windows. For example, an average of accidentals in time windows: [-6,-14] and [6,14] and subtract from the red filled peak, to remove the accidentals.

- Beside these, we have some contamination from ep$\rightarrow e'\Delta\gamma$ and ep$\rightarrow e'N\gamma\pi$. In both of these cases, the missing mass may be comparable to that of the DVCS event due to the resolution effect. The former can be subtracted from the knowledge of its cross section which is an order of magnitude smaller than the DVCS cross section. Contribution from later one can be minimized by using the tight and safe cut on M_x^2 $(M_x^2 < (M_p + M_{\pi^0})^2)$. To make such a tight cut first the tail and width on missing mass distribution is reproduced using Monte-Carlo with the same cut as in data $(M_x^2 < (M_p + M_{\pi^0})^2)$. Then the missing

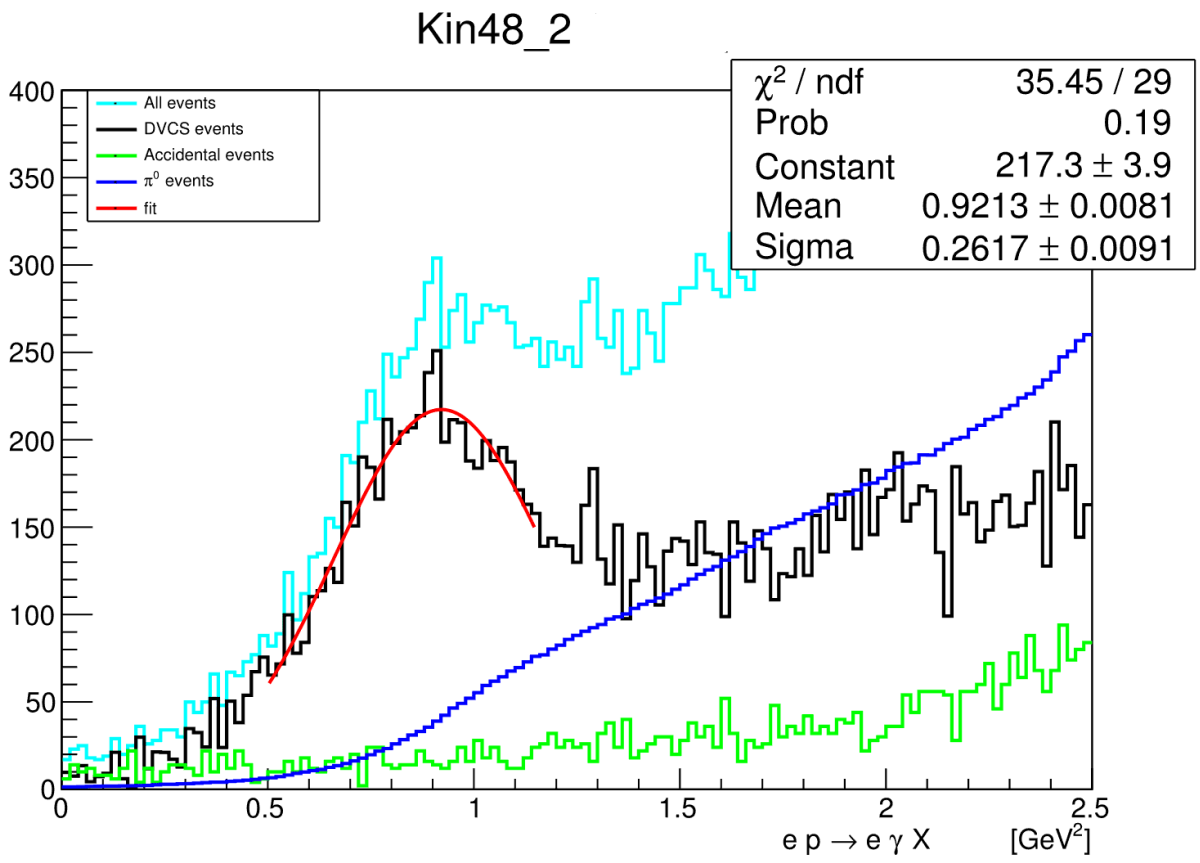

Figure 9: *The missing mass squared distribution of final hadron for one of the kinematic (48_2). To ensure exclusivity the recoiled proton is reconstructed by using the missing mass technique. The Cyan histogram is for all the events H(e,e'γ)X, blue one is for π^0 events H(e,e'π^0)p, green is for accidentals coincidences while black is for the events after accidentals and π^0 subtraction.*

mass distribution is fitted up to 1.1 GeV^2 to get the estimate of the background under the cut $M_x^2 = (M_p + M_{\pi^0})^2$. In the case of E00-110 the background below $M_x^2 = (M_p + M_{\pi^0})^2$ is only 1.71% of total [26].

4 Jefferson Laboratory

This experiment was done in Hall A of Jefferson Laboratory, located in Newport News, Virginia. We used longitudinally polarized electron beam from Continuous Electron Beam Accelerator Facility (CEBAF), which was upgraded from 6 GeV to 12 GeV in 2014. CEBAF has two superconducting linacs to accelerate the beam. The source of an electron is Gallium Arsenide crystal doped with Phosphorus (GaAsP). As the polarized laser beam strikes the GaAsP crystal placed in an ultra vacuum chamber, polarized electrons are ejected [27] due to the photoelectric effect. The ejected electrons are first accelerated up to 45 MeV, then injected into North linac for further acceleration. At the end of North linac, the beam is steered by magnetic arcs to South linac. Once the beam passes through each linac, it completes one pass. In a single pass, the beam is energized up to 2.2 GeV (12 GeV configuration). In this way, the beam can be

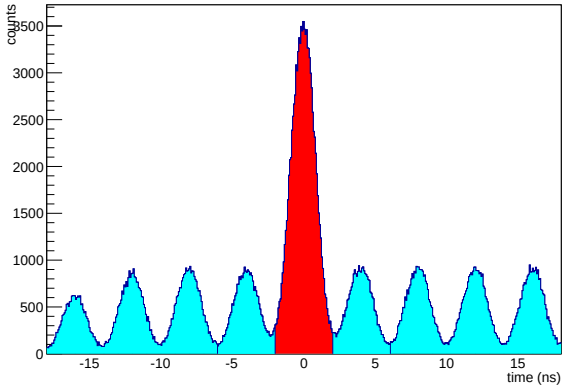

Figure 10: *Coincidence time spectrum of the events with 4ns CEBAF beam structure. The red peak shows the events within our coincidence window. To subtract the accidental events from red peak one can take the average of accidental events between any two different time windows as [-6,-14] and [6,14].*

recirculated in the linacs maximally up to 5 complete passes. The experimental Halls A, B, and C can get the maximum beam energy up to 11 GeV while due to the position of Hall D (see Figure 11), beam can be passed through one extra linac before delivering to Hall D. Therefore, only one experimental Hall i.e D can reach up to 12 GeV, the maximum value. The main features of this facility which are crucial to our experiment are the beam polarization, duty factor, and luminosity. The preliminary result from Fall 2016, showed the beam polarization of 85% [28]. This facility can deliver a beam with high duty factor (250 MHz) which is important for the coincidence experiments like us to minimize the background from random coincidences. In addition to these two features, we can also get the high beam luminosity $\sim 10^{37} cm^{-2} s^{-1}$.

4.1 Experimental Hall A

In this section, we will discuss the Hall A basic instruments which are important to our experiment.

4.1.1 Beam line

Let us start with beam line components. For the beam polarization measurement, there are two polarimeters: Compton Polarimeter which is located at the entrance of Hall and Moller Polarimeter at few meters before the target. The Compton is the non-invasive way of measuring the polarization of electron beam in Hall while the Moller is the invasive one. The relative precision in polarization measurement is about 3.2% and 1.2% (at 4.5 GeV) for Moller and Compton respectively [27]. To monitor the beam position and direction at target location we have two Beam Position Monitors (BPMs). They can provide the relative positions of the beam within 100 μm for currents above $1 \mu A$ [29]. The beam energy is measured by an Arc method, which uses the knowledge of the deflection of the beam in the magnetic field produced by eight dipoles that steer the beam in an arc. The precision in energy measurement is $\delta E/E = 10^{-4}$ [30].

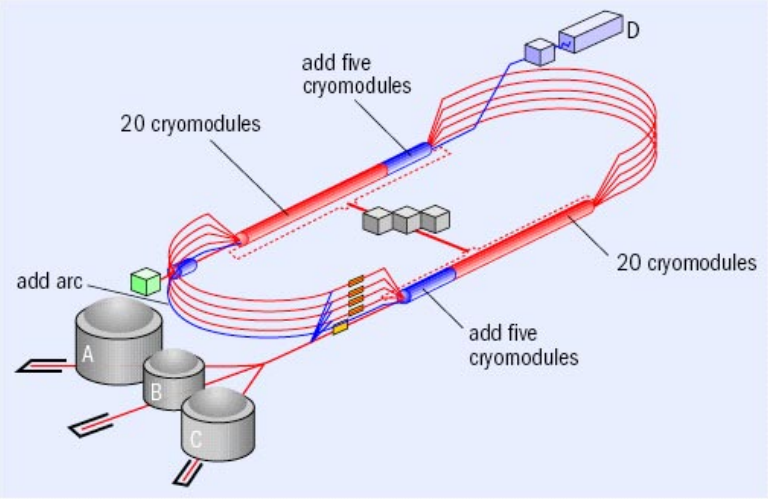

Figure 11: *Schematic diagram of CEBAF at Jefferson Lab. It can deliver the polarized electron beam up to 12 GeV. There are four experimental Halls. Hall A, B, and C can go maximum to 11 GeV but Hall D can reach up to 12 GeV when CEBAF is operating optimally. This figure was taken from Jefferson website (https://www.jlab.org).*

For the beam current and charge measurement, we have Beam Current Monitor (BCM) in the beam line. The schematic diagram of the BCM is shown in Figure 15. It consists of an Unser monitor, two RF cavities, associated electronics, and data acquisition system. The Unser monitor provides an absolute reference [31] to beam current. The Unser monitor is calibrated using the known current source and later used as a reference to calibrate the BCM. BCM can measure current down to $1\mu A$ with a relative accuracy of 0.5% [27]. For the precise measurement BCM needs to be calibrated frequently (about once in a month). I worked on BCM calibration, so in later section 6.1, I will discuss more about it. Last but not the least component in the beam line which is crucial for our experiment is a raster system. It is located upstream from the BCM system. The raster is basically magnetic coils which can move the beam in both horizontal and vertical directions. Typically, we use 2× 2 mm raster beam on Liquid Hydrogen target while running at around 20μA. With the rastered beam, the density fluctuation from the beam heating is limited to a few percent at a beam current of 100 μA.

4.1.2 Target System

The cryogenic target system is mounted inside the evacuated target chamber. We took data on Liquid Hydrogen (LH_2) target for this experiment. LH_2 is enclosed in 15 cm long and about $\sim$ 15 mm thick cylindrical aluminum target cell. The LH_2 target is operated at 19 K and 0.17 MPa for a density of 0.0723 g/cm^2 [27]. Along with cryogenic target, the target system also consists of a dummy target and another five solid targets. All these targets are arranged in a vertical stack and can be controlled remotely to select the target on beam path. One of a solid target is the dummy target which is 15 cm aluminum cell without the LH_2 inside it. It helps to estimate the scattering contribution from an Al window enclosing LH_2. Another solid target is multi-foil carbon target which is used for optics calibration of the spectrometer. The other solid targets like carbon hole, BeO, and raster are used for beam centering purposes.

4.1.3 The High Resolution Spectrometers (HRS)

The Hall A consists of a pair of identical HRS, one in left (LHRS) and the other at right side (RHRS) of the beam direction. The momentum range of each of a spectrometer is 0.3 - 4.0 GeV/c with the acceptance of 4.5% with respect to the central momentum i.e -4.5% $< \delta P/P_0 <$ +4.5%. One of its main feature is high momentum resolution of the order of 10^{-4}, between the range 0.8 to 4.0 GeV/c. The other features are good position ($\sigma_{x(y)} = 1$mm) and angular(σ_θ) = 0.5 mrad) resolution [27]. The HRS consists of three quadrupoles (Q) and a dipole (D) in the configuration QQDQ with a vertical bend. The schematic layout of the HRS magnet is shown in Figure 12.

The first two quadrupoles focus the particles into a dipole on the way towards the detector hut. As the charged particles enter a dipole they get deflected depending on their momentum. Based on this fact, one can tune the suitable magnetic field in dipole (both magnitude and polarity) and select the particle of desired charge and momentum. These selected particles of our interest are then focused by the third quadrupole to the detector stack. The detector packages for both the HRS are almost similar and shielded against the background radiation by thick concrete blocks. The tracking information is provided by the pair of Vertical Drift Chambers (VDCs). Each VDC consists of two wire planes oriented 90^0 to each other. Its position and angular resolutions are about 100 μm and 0.5 mrad respectively. The two plastic scintillators S0 and S2 are basically used for triggering. The gas Cherenkov, filled with CO_2 at atmospheric pressure is mounted between the two scintillators S0 and S2. It allows distinguishing between electrons and pions. The threshold for pions to create the Cherenkov light is 4.8GeV/c while for an electron is 17 MeV/c [27]. The coincidence of a Cherenkov signal a scintillator S2 signal forms the main trigger for the DVCS experiment. At the end of the detector package, we have electromagnetic calorimeter (Pion Rejector). Pion Rejector consists of two layers, each of the layer consists of 34 identical lead glass blocks in left HRS, but for RHRS pion rejector is thicker than that of LHRS. On the basis of the energy deposition by electron and pion, we can reject/select pions. Because of being hadrons, pions deposit less energy in electromagnetic calorimeter. On the other hand, the electron deposits relatively high energy in the electromagnetic calorimeter due to electromagnetic interaction with the material of the calorimeter. The combination of gas Cherenkov and shower detectors can select the electron with about 98% efficiency [27]. The Hall A detector package consists of other detectors which are not discussed in this document as our experiment does not use them. However, further information can be found at [27].

5 DVCS Dedicated Instrumentation

As discussed earlier DVCS is three body final state with a photon as one of the final particle so, to detect the photon we have own DVCS dedicated calorimeter. Due to the proximity of the calorimeter to the beam line raw event rate on calorimeter is high up to 10 MHz [32] . So, to deal with the pile-up event in calorimeter we have the Analog Ring Sampler (ARS). ARS differentiates two photons if they are separated by more than 4ns [32]. In this section, we will discuss some of our dedicated instruments.

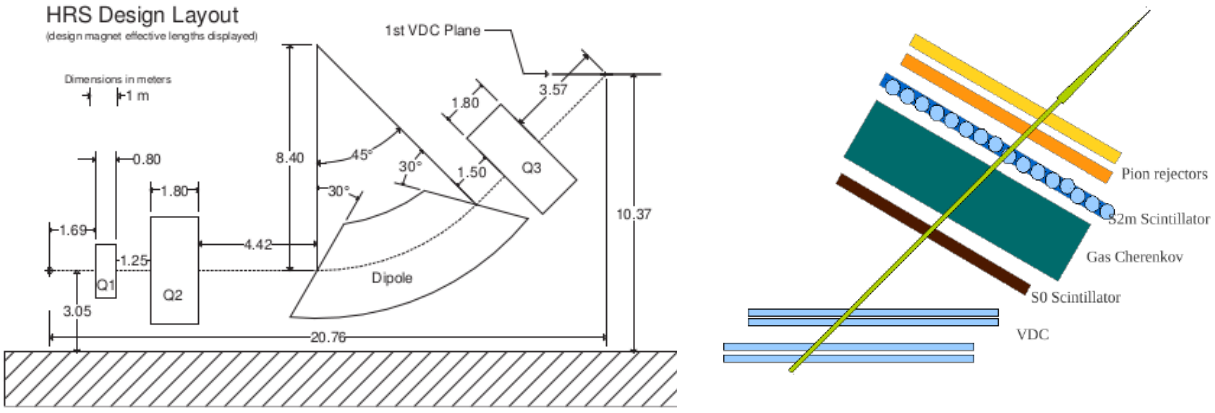

Figure 12: *Left: Schematic layout of the magnets in HRS. HRS is designed in QQDQ configuration [27]. Right: Schematic layout of the detector package. The direction of the arrow shows the nominal particle trajectory through detector stack. This figure was taken from [27].*

5.1 Calorimeter

Apart from the Hall A equipment, we have a dedicated electromagnetic calorimeter for photon detection. Calorimeter consists of 208 lead-fluoride (PbF_2) blocks arranged in 16 rows and 13 columns. The dimension of each block is $3 \times 3 \times 18.6\ cm^3$. As the photon passes through the calorimeter, it produces showers of electron-positron pairs. As the produced electron-positron pairs pass through the calorimeter material Cherenkov light is produced which is then collected by photo-multiplier tubes (PMTs). The PMT is connected to the end of each block. The Molière radius and the radiation length of PbF_2 are 2.2 cm and 0.93 cm respectively [8]. Therefore, the typical electromagnetic shower is contained within 9 adjacent blocks such that 90% of the energy of a photon entering the block is contained in that block. Due to the radiation damage, the resolution of calorimeter degrades with time. The energy resolution of calorimeter is about 3.6% at 4.2 GeV at the end of experiment E12-06-114 and the spatial resolution is 2 mm at 4.2 GeV [8].

5.2 The Analog Ring Sampler

The DVCS calorimeter is small in size. In order to have large acceptance, it needs to be placed close to the beam line and target. Moreover, we are running at high luminosity ($\sim 10^{37}\ s^{-1}\ cm^{-2}$). Due to these facts in some of our kinematics, the raw events on calorimeter are expected to be high around 10 MHz [26]. This high event rate results in pile-up events as shown in Figure 13. As a result, we can not fully rely on ADCs which typically integrate the signal within 60 ns window, especially if two or more signals arrives less than 60 ns window. In order to deal with this pile-up event we have Analog Ring Sampler (ARS) which digitized the calorimeter signal. The ARS [33] consists of 128 capacitors and samples the signal at a clock rate of 1 GHz. Once the sampling is done, the signal is stored in capacitors and then digitized if the signal passes the set software threshold.

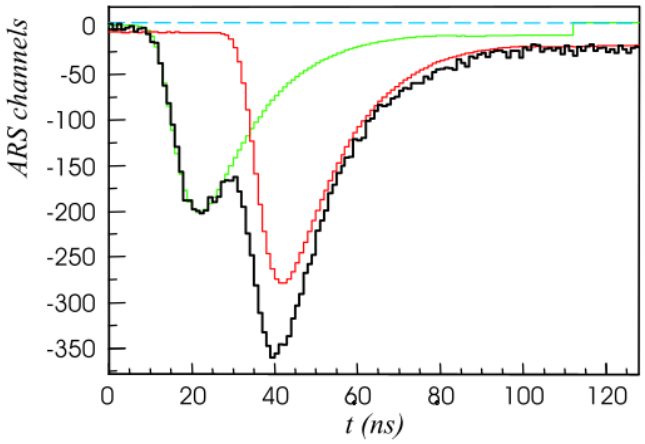

Figure 13: *ARS signals recorded in 128 ns window. ARS takes the snapshot of the signal every 1 ns. The black signal which we measure is the sum of red and green signals separated closely in time (few ns). Offline analysis of ARS signal allows one to extract the green and red signals from the black one with good time and energy resolution. The figure is taken from [26].*

5.3 Data Acquisition and Trigger

The Data Acquisition (DAQ) process uses the Cebaf Online Data Acquisition (CODA) developed by the JLab data acquisition group [27]. DVCS trigger logic is a two level decision. The first level trigger logic is formed by a scintillator (S2) signal and a Cherenkov signal in coincidence in HRS. A threshold is set on Cherenkov so that π^- triggering the S2 are rejected. When we have a good electron in HRS (coincidence between these two detectors) the Trigger Supervisor (TS) sends a stop signal to the ARS system then the signal is divided to ARS and ADCs. The ARS signal in each block of the calorimeter is integrated over 128 ns. Then the calorimeter trigger module computes the sum of the integrated ADCs signal for all 2×2 neighboring blocks for making the quick decision to trigger the event. If the integrated ADCs sum is above the set threshold then the VALID signal is sent to trigger supervisor and ARS data is recorded and ARS is reset. It takes 128 μs to digitize and transfer the ARS data [32]. Otherwise, if the ADCs integrated sum from calorimeter trigger module does not pass the threshold then ARS signals are cleared within 500 ns and DAQ gets ready for a new signal. . The schematic of DVCS trigger is shown in Figure 14.

6 My Contribution to DVCS

I have joined Ohio University in Fall 2014. After completing the core course, I joined Dr. Roche's research group in May 2015. For the first 3 months of that summer, I worked on the analysis of simulation for the JEF experiment in Hall D at Jlab. Then from Fall 2015 I joined the DVCS collaboration, it is the group of around 20 physicists (Faculty + students) from different institutions working on GPD program at Jefferson Lab. Since then I am one of an active member of this group. I attended "APS April meeting 2017" on behalf of our collaboration and presented the status of our experiment (slides for this talk are in Appendix

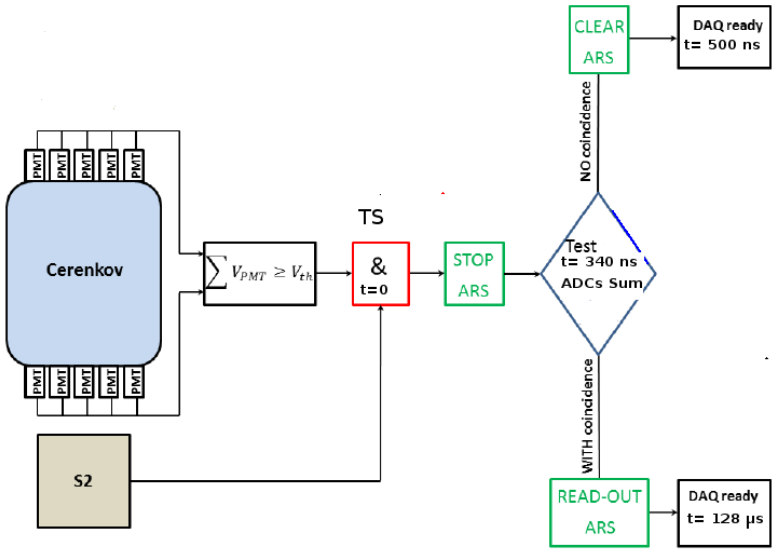

Figure 14: *Schematic diagram of DVCS Trigger. At first, it looks for coincidence between scintillator S2 and Cherenkov in HRS. At second level, it computes the integrated ADCs signal in 60 ns time window for every signal passing the first logic. ARS signals are recorded or cleared depending on whether the integrated ADCs signal passes the set threshold or not. Figure is taken from [32].*

B). In 2016 I was mostly stationed at JLab for the preparation of our experiment and to help in taking a data. During this period, I took around 40 shifts each of 8 hours to help data taking. I was involved in calibrating the Beam Current Monitors (BCMs) and selecting the DIS events. I was also involved in stacking and de-stacking the calorimeter blocks and other similar issues related to our experiment when I was on site.

6.1 Calibration of Beam Current Monitors

Beam Current Monitor (BCM) is a low noise and stable instrument to measure the beam current. It consists of Unser monitor, two RF cavities (upstream (U) and downstream (D) with respect to the beam direction), the electronics and a data acquisition system [27]. The schematic layout of the BCM system in Hall A is shown in Figure 15. The Unser monitor/Parametric Current Transformer (P.C.T Toroids in Fig. 15) provides the absolute reference to beam current. To calibrate the Unser known DC current is passed through the calibration wire. Each of BCM has multiple receivers: analog and digital. U1 and D1, the analog receivers, does not amplify the signal from cavities while D3 and D10 are other analog receivers which amplify the signal from downstream cavity by 3 and 10 times respectively. We also have two new digital receivers Unew and Dnew. The output of each receiver is sent to Voltage to Frequency (V-F) converter and then to scalers such that at the end rates measured by the scalers are proportional to the current.

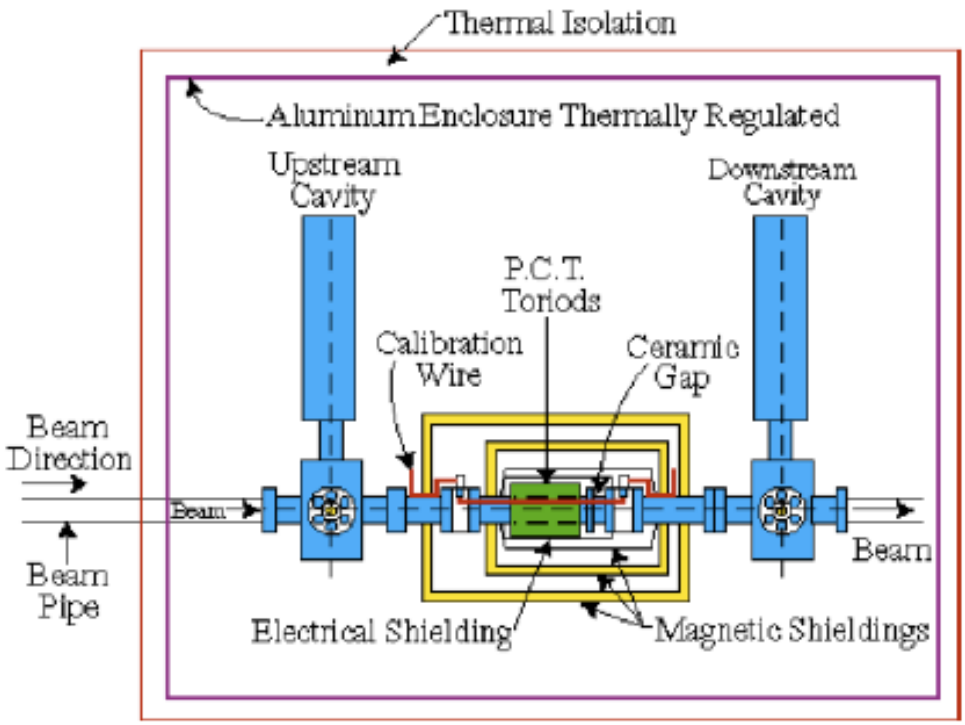

Figure 15: *Schematic layout of the Beam Current Monitor system in Hall A at JLab. The entire system is thermally isolated. The Unser monitor/Parametric Current Transformer (P.C.T Toroids) is placed in between the two RF cavities. A calibration wire passes through the beam line for Unser calibration. Figure is taken from [34].*

As the beam passes through the cavity, it induces the magnetic field within the cavity. The induced magnetic field is proportional to the beam current. The output signal from BCM gives a relative measurement of a beam current. For absolute current measurement, BCM is calibrated against the Unser current. Though Unser can measure current we cannot use it for a long time for data taking as its pedestal drifts in an unpredictable way over several minutes. Unlike the Unser, the BCM cannot be calibrated directly using DC current as it is an RF cavity and the cavity does not induce magnetic a field with DC source. So, BCM calibration is a two step process: First, the Unser calibration using known DC source current. Second, the BCM calibration using Unser as a reference.

6.1.1 Unser Calibration

Unser calibration is basically converting the Unser frequency to Unser current ($f_{Unser} \rightarrow I_{Unser}$). Unser is calibrated without beam in the Hall using the known direct current source from Hall A and this current is precisely known with relative uncertainty of 0.1% at 30 μA. The current in the wire is gradually increased from 0 to 100 μA in steps. Each increment in the current is followed by intervals with no current to capture the eventual fluctuation of the Unser's pedestal. For instance, current in the wire is changed as: 0, 5, 0, 10, 0, ...100, 0 μA. At each current setting, data are taken for about 1 minute. Then, first the average of local pedestal is measured and

is subtracted from the signal at each current. Then the pedestal subtracted Unser frequencies are plotted against the injected known current as shown in Figure 16. The slope of the fit gives conversion relation between Unser current and Unser frequencies as $I_{Unser} = slope \times f_{Unser}$.

Figure 17 shows the Unser pedestal varies up to 1 μA with time. So, during the Unser calibration the Unser pedestal is subtracted from Unser signal at each current setting to minimize the uncertainty.

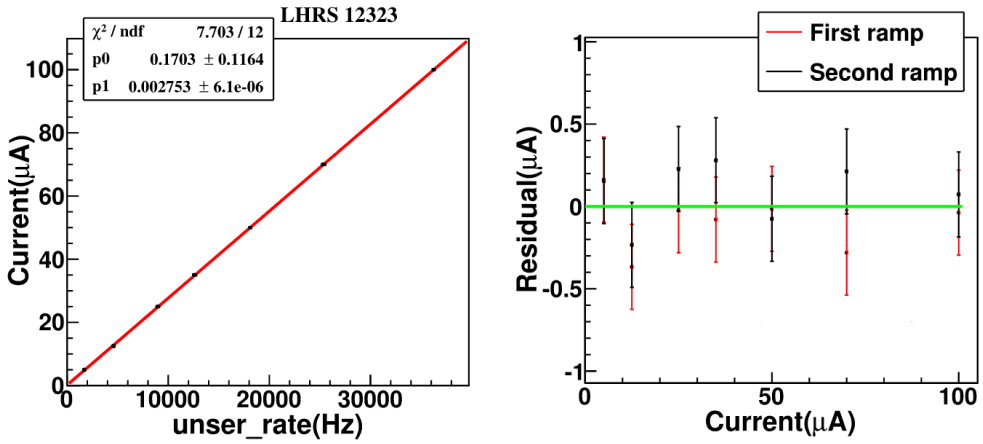

Figure 16: *The Unser calibration against the known DC current. Left: The pedestal subtracted Unser frequency is plotted against the known injected current. The right plot shows the fit for the residual at different current. To study the systematic fluctuation of Unser reading for each calibration two points were taken for each current setting.*

Period	**Run**	**Gain** $(10^{-6})\mu A/Hz$
Fall 2014	X	2755 ± 7
Spring 2016	21590	2754 ± 6
	12323	2753 ± 6
	22324	2753 ± 6
Fall 2016	23217	2506 ± 5
	23779	2504 ± 5

Table 3: *Stability of the Unser gain. Different colors represent different periods of time. The light gray is for Fall 2014, light cyan is for Spring 2016 and pink is for Fall 2016. The Unser gains are stable within the same period. The Unser gain during Fall 2016 is about 10% less than the rest period which is due to the unplugging one of the hardware component from Unser system.*

The uncertainty in Unser reading is mainly due to the variation in the Unser pedestal and can be evaluated in the following way. First, take a run with no beam and divide the entire Unser signal into many segments as shown in Figure 18. To resemble with the Unser calibration data, each segment corresponds to 1 minute in time scale. Then the uncertainty in each of the segments was computed as:

$$(\Delta I)_i = \left(\underbrace{\overline{P}_i}_{\text{Observed Pedestal}} - \underbrace{\frac{\overline{P}_{i+1} - \overline{P}_{i-1}}{2}}_{\text{Expected Pedestal}} \right) \times Unser\_Gain$$

where $\overline{P}_{i+1}$, $\overline{P}_i$ and $\overline{P}_{i-1}$ are the average Unser pedestals in the segments: i+1, i, and i-1 respectively. Figure 18 on Left shows the uncertainty in Unser pedestal in terms of current for a particular run 12813. We did a similar analysis for many runs and found the average uncertainty in Unser current reading to be 0.2 μA which is the precision used for each measurement on Figure 16.

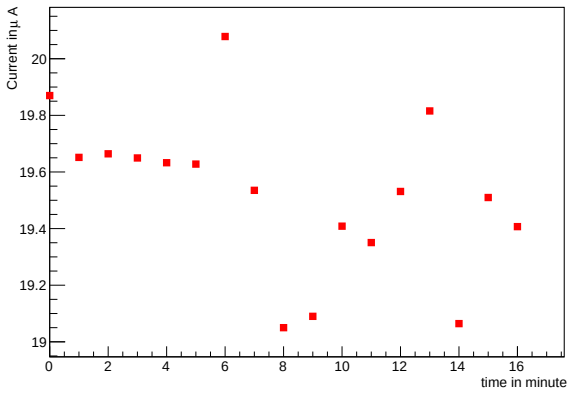

Figure 17: *Variation of Unser pedestal with time. Unser pedestal varies up to 1 μA within several minutes such that pedestal needs to evaluated at every minute of the data being taken to be valid.*

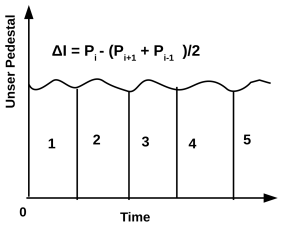

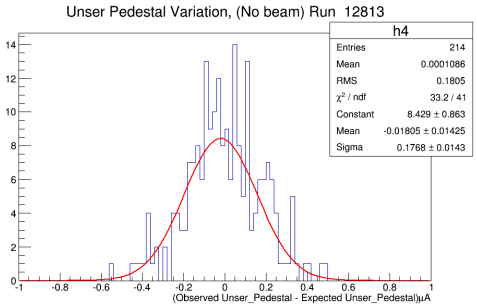

Figure 18: *Estimation of fluctuation of the Unser pedestal on the minute time scale. Left: Determination of Unser pedestal locally. The entire Unser signal is chopped into many segments, each of 1 minute in time. Right: Fitted uncertainty in Unser reading in terms of current for a particular run. The average uncertainty in Unser was found to be 0.2 μA.*

The whole idea behind BCM calibration relies on Unser calibration. So, to see any change in Unser gain, the Unser monitor is calibrated time to time. Table 3 shows the stability of Unser gain during different periods of data taking. The three different colors show different periods of data taking. The Unser gain is stable in each period. Drop in the Unser gain in Fall 2016 was due to the removal of an extra hardware component in Unser system.

6.1.2 BCM Calibration

Once the Unser is calibrated, its current is used as a reference to calibrate the BCM. A typical BCM calibration run is shown in Figure 19. The beam current is gradually increased in steps. Each beam on period is followed by a beam off period to account the Unser pedestal fluctuation. For the BCM calibration, BCM frequency is plotted against the Unser current and then fitted with a straight line. Each of the BCM receivers is linear within the certain current range so the fitting range is different for each of these BCM receivers. For example, D3 is linear from 0-60 μA whereas D10 is linear from 0-25 μA etc. The typical BCM calibration is shown in Figure 20. In the same way, all the 6 BCMs U1, D1, D3, D10, Unew, and Dnew are calibrated. Once we get the fitting parameters the BCM frequency can be mapped to current as:

$$I_{BCM} = f_{BCM} \times \text{gain} + \text{offset} \tag{14}$$

where I_{BCM} and f_{BCM} are current and the frequency of the BCM.

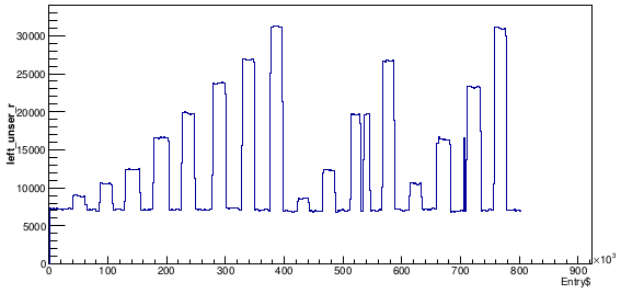

Figure 19: *Example of the BCM calibration run. The Unser rate is shown as the function of time. Each beam on period is followed by beam off period for better estimation of the Unser pedestal.*

The BCM needs to be calibrated from time to time, usually once or twice a month to see if there is any shift in gain. We found that for the analog BCM receivers D1, U1, D3, and D10 the gain was constant within statistical uncertainty within a run period for e.g. Fall 2016. So, for these analog receivers, we decided to use the global calibration coefficients for current and charge determination. In global calibration, for each of the BCM receiver, all the frequency readings from each calibration run from different beam periods (Spring and Fall 2016) are plotted against the corresponding Unser current at once to extract the single value of gain and offset. One example of global calibration is in Appendix A. Using global calibration coefficients agreement in charge measurement between different BCM receivers were reduced to 1% from 2% that we got from time specific calibration coefficients. For the digital receivers (Unew and Dnew) the gains changed from time to time so we need to use time specific calibration

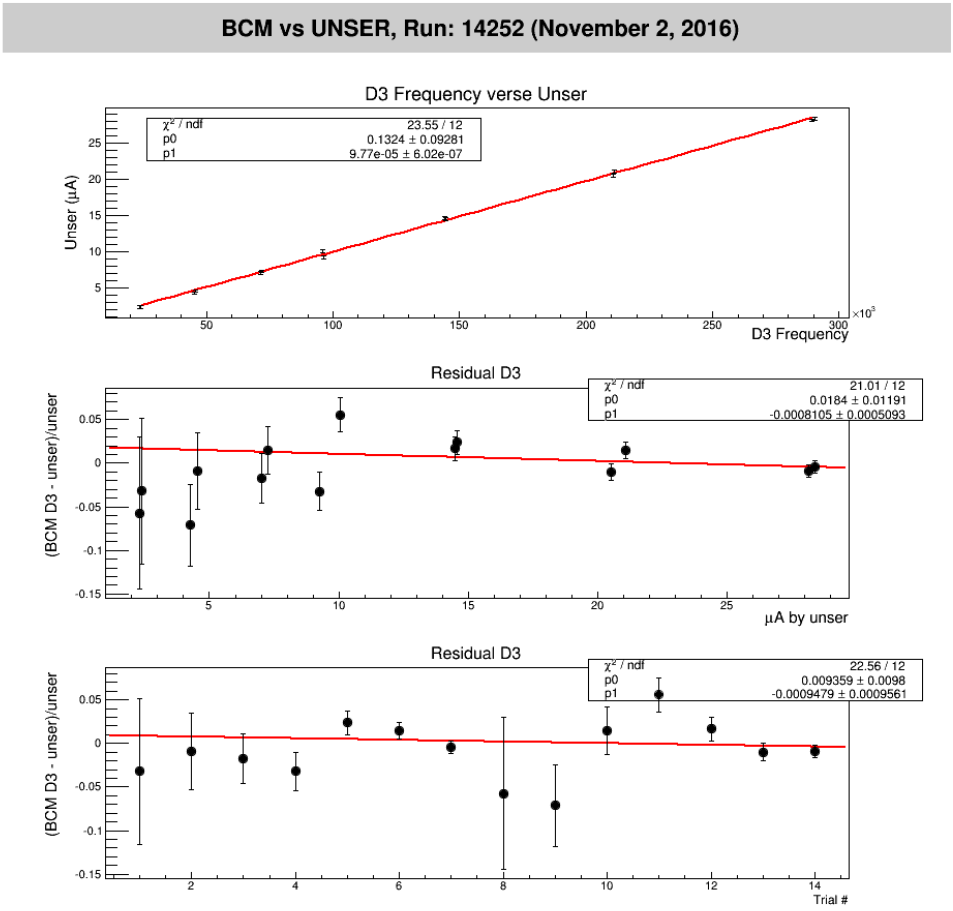

Figure 20: *Typical BCM calibration for the BCM receiver D3. At the top D3 frequency is fitted against Unser current within its linearity range 0 to 60 μA. The slope of fit gives the BCM gain. The middle plot shows the relative residual as the function of current. The bottom plot shows the residual for different trials.*

coefficients. All the coefficients for different BCMs for a different period of data taking are presented in Appendix A.

6.1.3 Charge Measurement

One of the main goals of our experiment is to measure the absolute cross section of DVCS process with high precision. For this, we need to know the number of incident electrons on the target precisely. For the total number of incident electrons, one needs to measure the total charge accumulated during the run. The charge (Q) is related to the number of incident particle (N) as: $Q = N \cdot e$, where e is the charge of the electron. The total charge can be computed by integrating the instantaneous current given by Equation 14 for each of the BCM

$$
\begin{aligned}
Q &= \int I(t)dt \\
&= \int (f_{BCM} \cdot \text{gain} + \text{offset})dt \quad \text{(using Equation 14)} \\
&= \text{gain} \times C + \text{offset} \times T
\end{aligned}
\tag{15}
$$

where C is total counts from scaler (BCM output) and T is the total duration of a run.

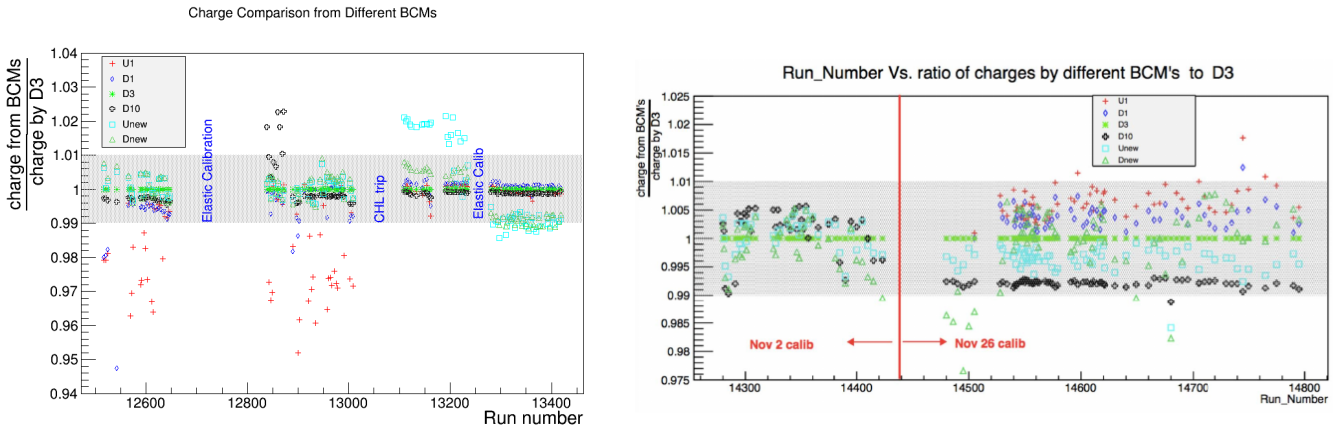

Figure 21: *Comparison of charge measured by different BCMs. The ratio of charge measured by different BCMs to the charge measured by D3 as the function of a run number. Left: Spring 2016. Right: Fall 2016. The shaded region shows ± 1% agreement between the charge measured by D3 and other BCMs.*

Figure 21 shows the comparison of charge measured by different BCMs. U1 (red points) is off by a few percent in the beginning of Spring 2016 (Left). The red vertical line on Right shows the distinction between two different calibration period. For the charge computation, the gain from the specific period was used. The gains for the new receivers are unstable and their electronics are noisy. The gain for D3 is stable and is linear in a wide range of current. So, we concluded to use D3 for the charge measurement.

6.2 Deep Inelastic Scattering Event Selection

Apart from the BCM and charge measurement I am also working on extraction of the Deep Inelastic Scattering (DIS) cross section. In this section, I will discuss on my preliminary analysis for the DIS cross section. DVCS (ep→e'pγ) is the subset of DIS (ep→e'X) process and DIS cross section is well known in our kinematic regime. Experimentally reproducing the DIS cross-section from our data ensure our understanding of luminosity as well as electron detection by the HRS. For this purpose in addition to the main DVCS trigger, a DIS trigger was used to capture the events that trigger the HRS irrespective to calorimeter triggering(see Figure 14). The experimental differential DIS cross section is given by:

$$
\frac{d\sigma}{d\Omega dE} = \boxed{\frac{N \times P}{LT \times Q}} \times \frac{1}{y_{tg} \times \eta_{virt} \times \eta_{exp} \times \Gamma_{DIS}}
\tag{16}
$$

track	z-vertex + track	PID + z-vertex + track	DIS + PID + z-vertex + track
0.62	0.57	0.50	0.49

Table 4: *Fraction of events left after the analysis cut.*

where N, P, LT, Q are the number of raw DIS events, prescale, live time and charge respectively. The other terms are:

- y_{tg}: target luminosity.
- η_{virt}: the term correcting the radiative effects.
- η_{exp}: a factor correcting for the event losses by the inefficiency of trigger and analysis cut.
- Γ_{DIS}: phase space in which the events are detected.

Each term in the rectangular box will be different from one to another run while the other terms are constant for the particular kinematic setting. From here, we will use the term "DIS normalized rates" to represent the term in a rectangular box. In principle, the DIS normalized rate should be constant within the same kinematics. Here, we present how we calculated each term in the DIS normalized rate.

1. N: the number of raw DIS events selected through the analysis cut. The analysis cut demands that the good scattered electron satisfying the following selection (still working on optimization of our cut):

   - Single track in VDC to remove the ambiguous case of multi-track when we do not know which is a good one.
   - Cut on the Z-vertex of target to ensure that scattered electron is coming from the LH_2 and not from the target cell wall (Al).
   - PID cut (combination of Cherenkov and Pion Rejector) to identify e^- and reject pion.
   - Events triggered by DIS trigger, formed by combination of a Scintillator and a Cherenkov (S2M & CER) in coincidence.

   Table 4 shows the fraction of events left after the analysis cut.

2. LT (Live Time), it is the total time when DAQ is available to process the data. Sometimes the events of interest may strike the detector when DAQ is busy processing the former event. In that case, we will miss that event. Live time correction factor is given as:

$$LT = \frac{\text{No. of Event Saved}}{\text{Total Events Firing the Trigger}}$$

3. P, the prescale factor. To have a control on a live time of the system we choose a prescale factor in each of our trigger settings. This prescale factor allows us to save only a fraction of the events firing the trigger. This helps us to keep the dead time low. For instance, with a prescale factor of 4, only one out of 4 events firing the trigger is saved in the tape.

4. Q is the charge accumulated during the run. It is measured using the BCM D3 as discussed in section 6.1.3.

In Spring 2016 we ran with different coincidence triggers setting formed by the combination of two scintillators (S0 and S2M) and Cherenkov (CER) (see Figure 14). The different coincidence trigger combinations are:

- S0&S2M (two scintillators S0 and S2M in coincidence).
- S0&CER (One scintillator and Cherenkov in coincidence).
- S2M&CER (Other scintillator and Cherenkov in coincidence (DIS trigger)).

For each event, "triggerPatternWord" is saved. The "triggerPatternWord" gives information about the trigger status. The lowest six bit of "triggerPatternWord" record the single raw triggers (e.g. S0, S2, Cherenkov etc) while remaining higher bit record coincidence triggers (e.g. S0&CER , S0&S2M etc). Depending on the masking value used to decode the "triggerPatternWord" one can know which trigger (single or coincidence) was fired for each event.

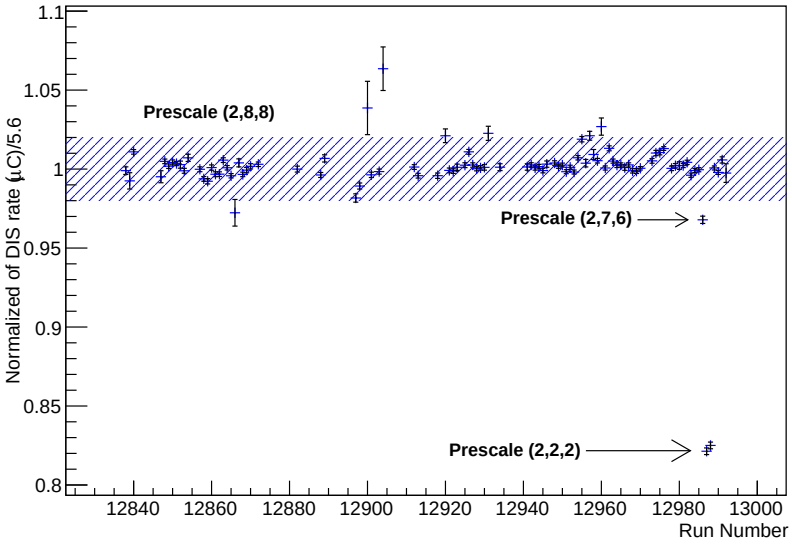

Figure 22: *Normalized DIS rate as the function of run number for kinematic* 48_3. *For simplicity, the normalized DIS rate is scaled with the average rate [5.6 events per* μC*]. The prescales shown are for the coincidence triggers S2M&CER, S0&CER, and S0&S2M respectively. The DIS rate from one run to another run agrees within* $\sim$ *2%. Details on discrepancy in of some of the data points are presented in the text.*

Figure 22 shows Normalized DIS rates for different runs of kinematic 48_3 taken in Spring 2016. Points with big error bar are for shorter runs (less than 5 min) which we will exclude in our final analysis. Normalized DIS rates are in agreement with each other within 2% (

band) as long as we have given combination on our coincidence triggers (S0&CER, S0&S2M, and S2M&CER). Surprisingly the normalized DIS rates changes with the change in prescale combination of our coincidence trigger. For instance, moving from the prescale combination of (2,8, 8) to (2, 2, 2) in S0&CER, S0&S2M, and S2M&CER respectively the DIS rate changes by $\sim$ 18%. We saw the same kind of effect in all kinematic taken in Spring 2016 and for every kinematics we have about 10% runs with a different combination of prescales setting on S0&CER, S2M&CER,and S0&S2M. In this period of data taking multiple aspects of the trigger configuration (eg prescale and threshold) were changed at once. This made it difficult to understand this effect. In the beginning of Fall 2016, we took a trigger test run, where we changed aspects of trigger configuration one at the time. From test run, we concluded that the prescale on S0&CER had only impact on the DIS rate. Less the prescale on S0&CER more the DIS events were missed. This means when S0&CER gets fired the event may not be tagged as DIS event despite being DIS event. At the end of a day, we came up with an idea of searching missed DIS events from the events triggered by S0&CER. The events which were triggered only by S0&CER had a signature on all of our detectors S0, S2M and CER (in individual detector signal) and with S2 and Cherenkov in coincidence were termed as missing DIS events. Finally, we corrected our final DIS rate by adding this missing DIS rate as:

$$Corrected\_DIS\_rates = DIS\_rate + Missing\_DIS$$

Table 3 shows after correction the DIS rates are in agreement below 2% even for the runs with different prescales on SO&CER. This works well for every kinematics. In Table 3 the prescale are in order of S0&CER, S0&S2M, DIS trigger and DVCS trigger respectively. The fifth column ("corrected DIS (PS+LT)") is the DIS events only corrected with live time and prescale factor. "Missing S2" in the sixth column stands for missing DIS rates. The last column shows the ratio of corrected DIS rates (with missing) to the average rate for comparison.

To reconstruct the event with precision, the event must pass through the acceptance region of the HRS. We are working on the acceptance of HRS. Once, we have acceptance region defined, we will implement it on our DIS event selection criteria. Then extract the DIS cross section to check the quality of data.

7 Thesis Goals

I completed my core courses in 2015 and in the same year I joined Dr. Roche's research group. I finished some mandatory classes like Computational Physics, Nuclear and Particle Physics (II) and Graduate Laboratory. I still need to take 3 more courses. My plan is to finish the remaining 3 courses within next one year. My thesis goals are: to measure both polarized and unpolarized the DVCS cross section for one of the x_B scan listed in Table 2. This is one of DVCS goals discussed in section 3. Table 5 summarizes the estimated timeline for the completion of purpose work and dissertation writing.

Run No.	Prescale	Live Time	Raw dis rate /μC	Corrected DIS PS+LT	Missing S2	Corrected DIS /μC	DIS / 5.63
				KIn48_3 (Spring 2016)			
12985	(8,8,2,1)	0.98	2.76	5..63 ± 0.02	0.01 ± 0.00	5..63 ± 0.02	1.00 ± 0.005
12986	(6,7,2,1)	0.99	2.74	5.45 ± 0.02	0.03 ± 0.00	5.54 ± 0.02	0.984 ± 0.005
12987	(2,2,2,1)	0.98	2.38	4.86 ± 0.02	0.86 ± 0.01	5.72 ± 0.02	1.016 ± 0.005
12988	(2,2,2,1)	0.98	2.39	4.88 ± 0.02	0.85 ± 0.01	5.73 ± 0.02	1.016 ± 0.005
				KIn48_4 (Spring 2016)			DIS/4.09
13279	(8,8,3,1)	0.98	1.01	4.12 ± 0.00	0.01 ± 0.00	4.13 ± 0.00	1.01 ± 0.00
13121	(4,2,3,1)	0.97	0.85	3.51 ± 0.04	0.61 ± 0.01	4.12 ± 0.04	1.01 ± 0.006
13123	(4,2,2,1)	0.97	1.72	3.44 ± 0.02	0.60 ± 0.00	4.04 ± 0.03	0.988 ± 0.006
13101	(3,3,2,1)	0.97	1.84	3.79 ± 0.02	0.30 ± 0.01	4.09 ± 0.03	1.00 ± 0.006
13364	(6,6,2,1)	0.97	1.95	4.02 ± 0.04	0.03 ± 0.00	4.05 ± 0.04	0.990 ± 0.006
				Kin48_1(Spring 2016)			DIS/6.42
12525	(8,0,3,1)	0.98	1.61	6.57 ± 0.04	0.00 ± 0.00	6.57 ± 0.04	1.02 ± 0.004
12570	(8,2,2,1)	0.98	2.8	5.71 ± 0.02	0.71 ± 0.00	6.42 ± 0.02	1.00 ± 0.003
				Kin48_2(Spring 2016)			DIS/19.10
13194	(8,8,3,1)	0.97	4.68	19.30 ± 0.13	0.04 ± 0.0	19.34 ± 0.13	1.012 ± 0.021
13195	(8,8,3,1)	0.97	4.67	19.28± 0.04	0.04 ± 0.00	19.32± 0.04	1.012 ± 0.015
13001	(8,8,2,1)	0.96	9.15	19.06 ± 0.04	0.04 ± 0.00	19.10 ± 0.04	1.00 ± 0.015
13183	(4,4,3,1)	0.96	4.34	18.10 ± 0.04	0.59 ± 0.00	18.70 ± 0.04	0.980 ± 0.015

Figure 23: *Correction for the normalized DIS rates for different kinematics taken in Spring 2016. In each kinematic few random runs with different prescale on S0&CER, S0&S2M were chosen and corrected DIS rates were computed. The normalized DIS rates are in agreement within 2% or less.*

Activity	**Estimated Future Timeline**
Fall 2015	Joined DVCS collaboration took mandatory classes
Spring 2015	At JLab to help data taking and BCM calibration
Summer 2015	Analysis on DIS event selection
Fall 2016	At JLab to resume the data taking; BCM analysis
Spring 2017	Back to Athens, Prospectus and class
Summer 2017	DVCS Simulation and Summer School
Fall 2017	Class and data analysis
Spring 2018	Remaining class and Data analysis
Summer 2018	Data analysis
Fall 2018 - Spring 2019	Data analysis; dissertation writing
Fall 2019	Ph.D defense; final document prepared

Table 5: *Estimated future timeline for graduation.*

8 Appendix A

8.1 Global Calibration coefficients

Table 6 and 7 shows the global calibration coefficients for Fall 2016 and Fall 2014. During Fall 2014, there were no any digital receivers. Figure 7 shows the global calibration coefficients for Spring 2016. The gain for new receivers changed multiple time, so one needs to use time specific calibration coefficients for them. Figure 6 shows an example of the global calibration of D1. The BCM frequency is plotted against Unser current from all the calibration runs at once to extract the BCM gain. As D1 is non linear at low current so the data is fitted above 7μA.

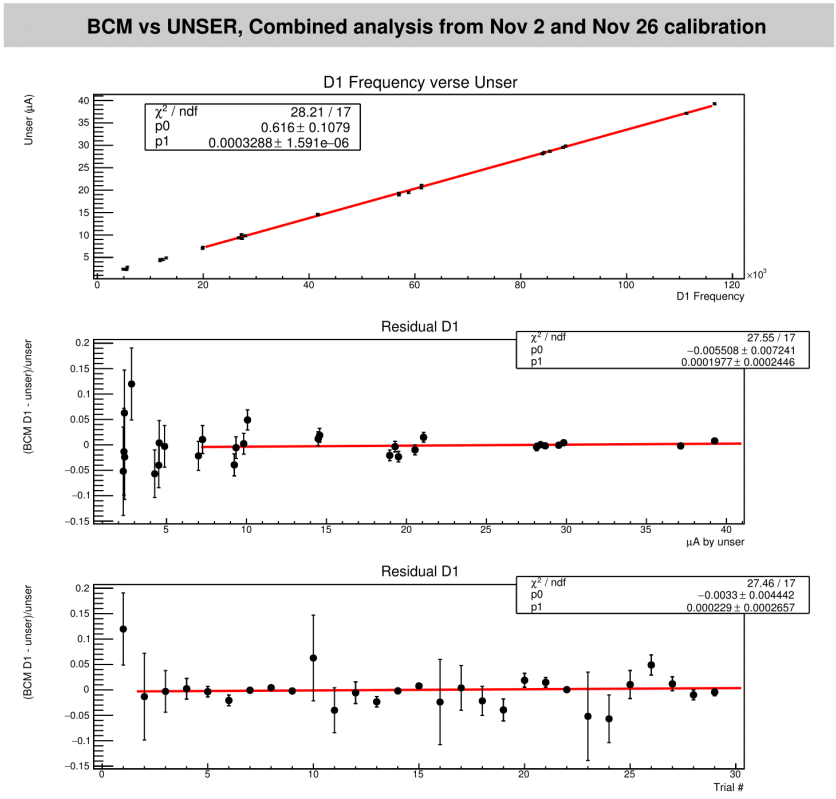

Figure 24: *An example of global calibration for D1. The BCM frequency is plotted against the corresponding Unser current from all the BCM calibration runs at once. The fit gives the single gain and offset for each of the BCM. D1 is not linear at low current so we fit the data above 7μA.*

BCMs	**Gain** ($\times 10^{-6}$) **(μA/Hz)**	**Offset** (μA)
U1	384.84 ± 1.86	1.10 ± 0.11
D1	328.77 ± 1.59	0.62 ± 0.11
D3	97.05 ± 0.32	0.19 ± 0.06
D10	33.72 ± 0.22	0.03 ± 0.08
Dnew	224.23 ± 0.74	-0.01 ± 0.06
Unew	255.50 ± 0.85	0.05 ± 0.06

BCMs	**Gain** ($\times 10^{-6}$) **(μA/Hz)**	**Offset** (μA)
U1	515.9 ± 9.99	0.56 ± 0.29
D1	454.53 ± 8.8	0.55 ± 0.22
D3	127.4 ± 1.6	0.39 ± 0.17
D10	45.65 ± 0.57	0.31 ± 0.17

Table 6: *Global calibration coefficients for different BCM receivers. Left: Global calibration coefficients for Fall 2016. Right: Global calibration coefficients for Fall 2014. There were no any digital receivers in Fall 2014.*

BCMs	**Gain** ($\times 10^{-6}$) **(μA/Hz)**	**Offset** (μA)
U1	351 ± 0.72	0.75 ± 0.05
D1	319 ± 0.65	0.62 ± 0.06
D3	93.09 ± 0.18	0.30 ± 0.05
D10	32.14 ± 0.18	0.19 ± 0.05
For runs between 12508 and 13015		
Dnew	172.15 ± 0.66	0.19 ± 0.06
Unew	199.25 ± 0.76	0.20 ± 0.06
For run between 13100 and 13261		
Dnew	249.95 ± 1.41	0.10 ± 0.12
Unew	295.64 ± 1.66	0.20 ± 0.12
For run between 13279 and 13418		
Dnew	42.94 ± 0.25	0.04 ± 0.12
Unew	50.05 ± 0.29	0.05 ± 0.12

Table 7: *Global calibration coefficients for Spring 2016 beam period. The analog BCM receivers had stable gain through the experiment (Fall and Spring 2016) so one global calibration coefficients can be used. The gain for new digital receiver changed multiple times so we need to use the proper calibration coefficients for specific time or run.*

9 Appendix B

9.1 APS 2017 Presentation Slides

Deeply Virtual Compton Scattering (DVCS)
E12-06-114
Hall A at JLab

APS April Meeting
28 January 2017

Bishnu Karki
Ohio University
Athens, OH

Introduction:

- Key objective of Nuclear Physics is to understand the structure of nucleon in terms of quarks and gluons.
- Scattering of relativistic electron off the Nucleon is one of the most powerful tool for studying the Nucleon structure.

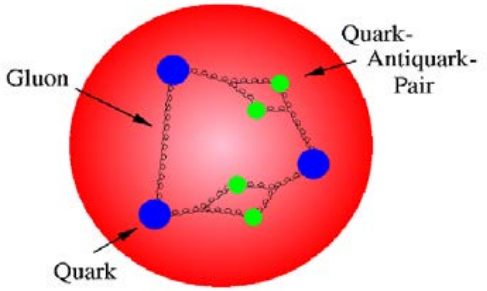

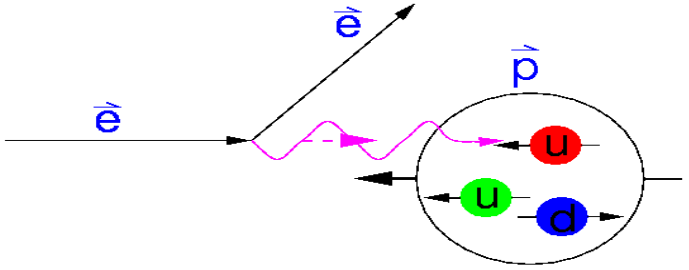

Generalized Parton Distributions (GPDs):

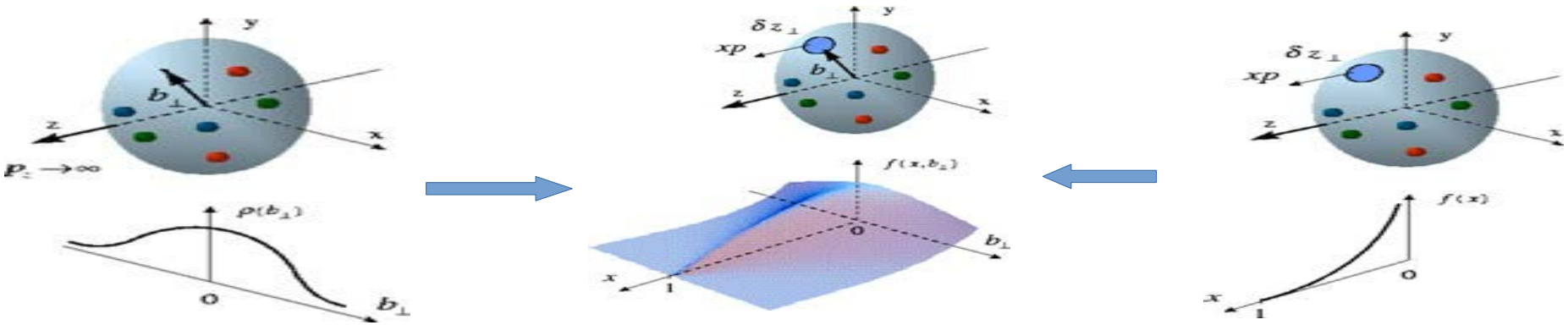

Elastic Scattering:
➔Proton extended object
➔**Form Factors (FFs)**
✔Spatial distribution
✗Longitudinal momentum distribution

Generalized Parton distribution (GPDs):
✔ Spatial distribution
✔ Longitudinal momentum distribution

DIS:
➔Discovered quarks
➔**Patron distribution functions (PDFs)**
✔ Longitudinal momentum distribution
✗Spatial distribution

GPDs allows to access the 3D parton structure of Nucleon

Factorization and GPDs:

QCD Factorization allows to access GPDs in various exclusive reactions.

In the Bjorken Limit $Q^2 = \begin{matrix} -q^2 \\ \nu \end{matrix} \begin{matrix} \to \\ \to \end{matrix} \begin{matrix} \infty \\ \infty \end{matrix}$ $\Big\}$ $x_B = \frac{Q^2}{2M\nu}$ fixed

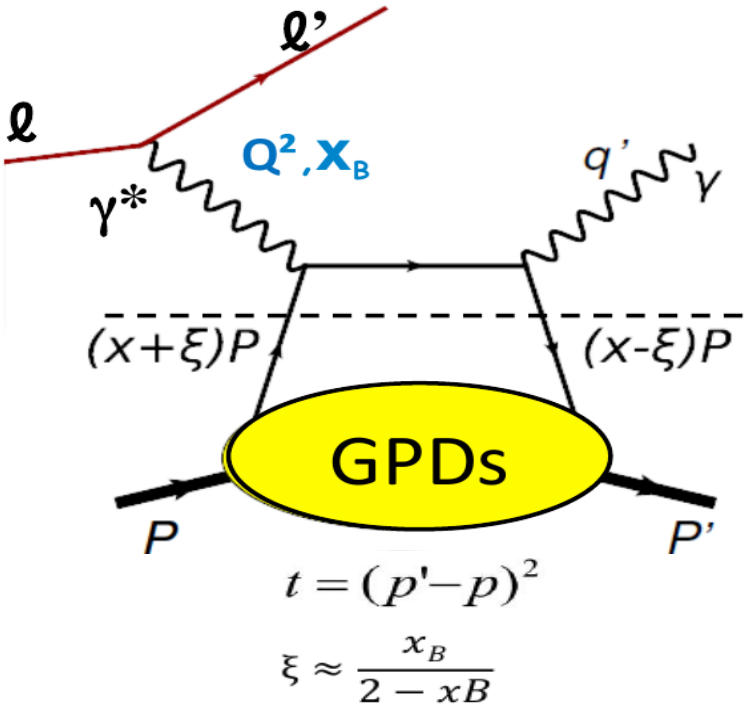

Hard Part
LO: QED
NLO: pQCD

Factorization

Soft Part
Non perturbative QCD
Parametrized by GPDs

Nucleon Helicity

	Conserving	Non-conserving
Unpolarized GPDs	H	E
Polarized GPDs	$\widetilde{H}$	$\widetilde{E}$

Minimal Q^2 at which factorization holds must be tested

DVCS and Bethe -Heitler (BH):

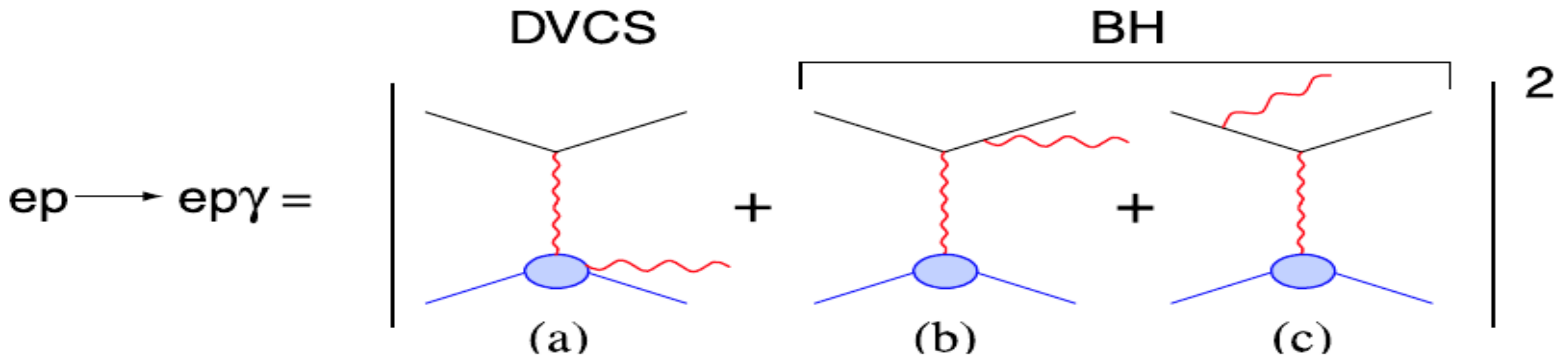

At leading twist

$$d^5\overrightarrow{\sigma} - d^5\overleftarrow{\sigma} = \Im m\,(T^{BH}\cdot T^{DVCS})$$

$$d^5\overrightarrow{\sigma} + d^5\overleftarrow{\sigma} = |BH|^2 + \Re e\,(T^{BH}\cdot T^{DVCS}) + |DVCS|^2$$

Known to 1%

Linear combinations of GPDs

Bilinear combinations of GPDS

Interference with BH gives access to Re and Im part of DVCS amplitude

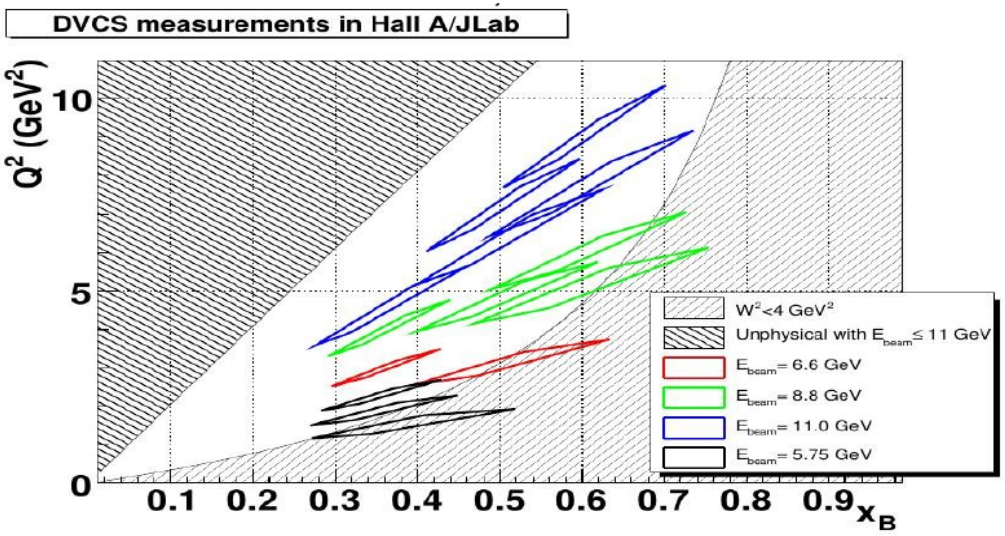

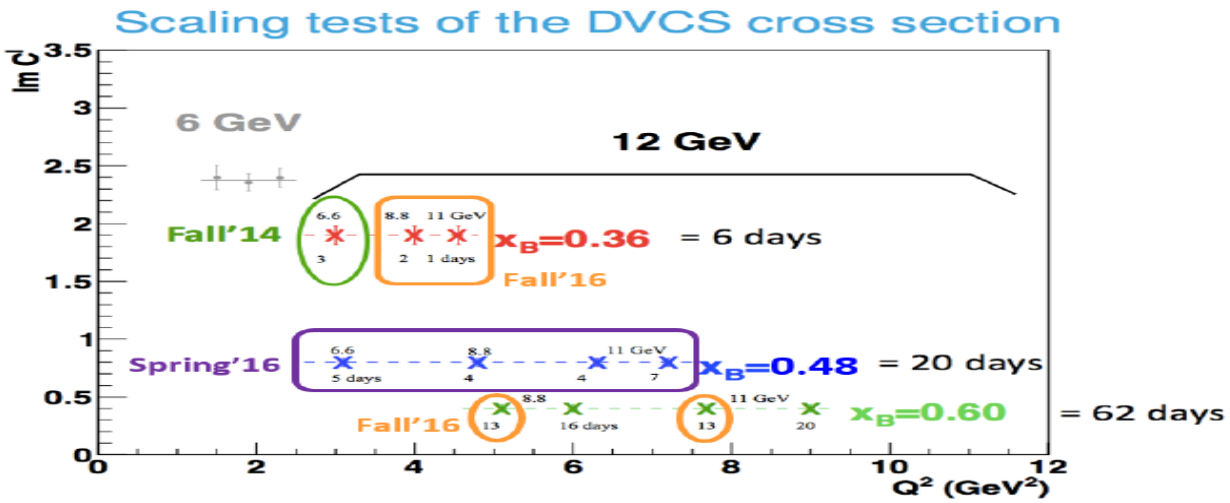

DVCS in Hall A:

✓E00-110/E03-106 (2004) ➡ first dedicated experiment (Q^2 dependence study)

✓E07-007/E08-025 (2010) ➡ Q^2 and beam energy dependence

✓E12-06-114 ➡
- Wider Q^2 scans at several x_B
- Absolute cross section ~5% relative precision

~50% of PAC allocation completed between 2014 and 2016

Jefferson Lab and 12 GeV Upgrade

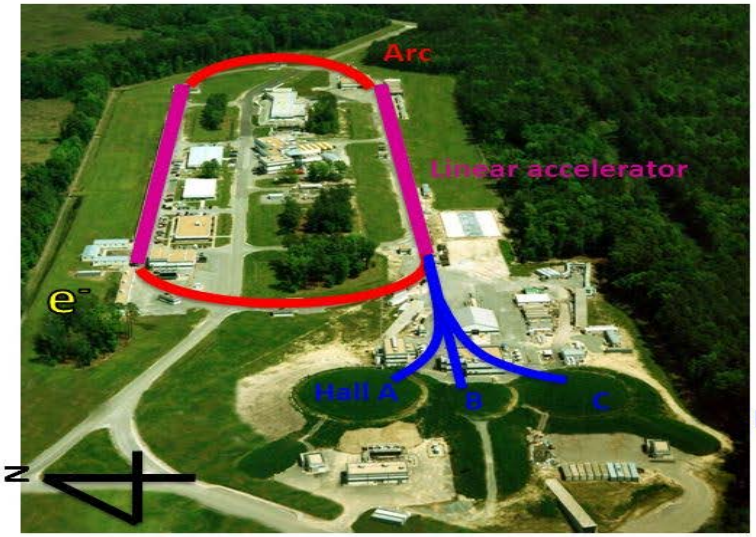

Aerial view of Jefferson Lab

Recirculating linear accelerator

Beam energy upgrade
from 6 GeV to 12 GeV

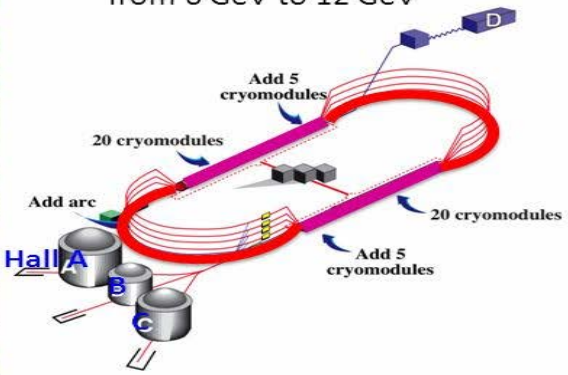

12 GeV Upgrade project

3

- **Beam dump commissioning**
- **5 pass, 2.1 GeV/pass**
- **High beam polarization (85%)**
- **Up to 80 μA (single Hall)**
- **Hall A, B and D running at same time**

- **Routine beam energy measurement (10^{-3} level)**
- **Upgraded raster system**
- **Upgraded Moller and Compton polarimetry**

DVCS is one first experiment to take data after 12 GeV Upgrade.

- High Resolution Spectrometer
  (P0 = 4.3 GeV, resolution 1x 10^{-4})
- Dedicated calorimeter.
  (Resolution 3.6 % at 4.2 GeV)

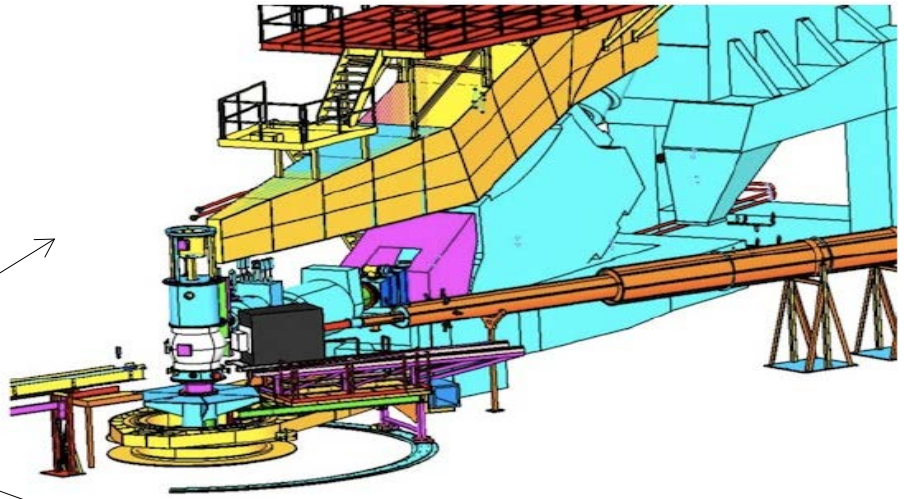

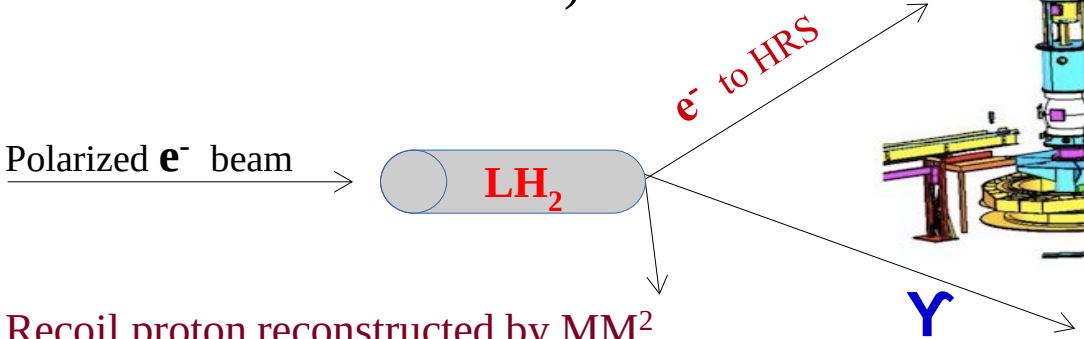

Recoil proton reconstructed by MM^2

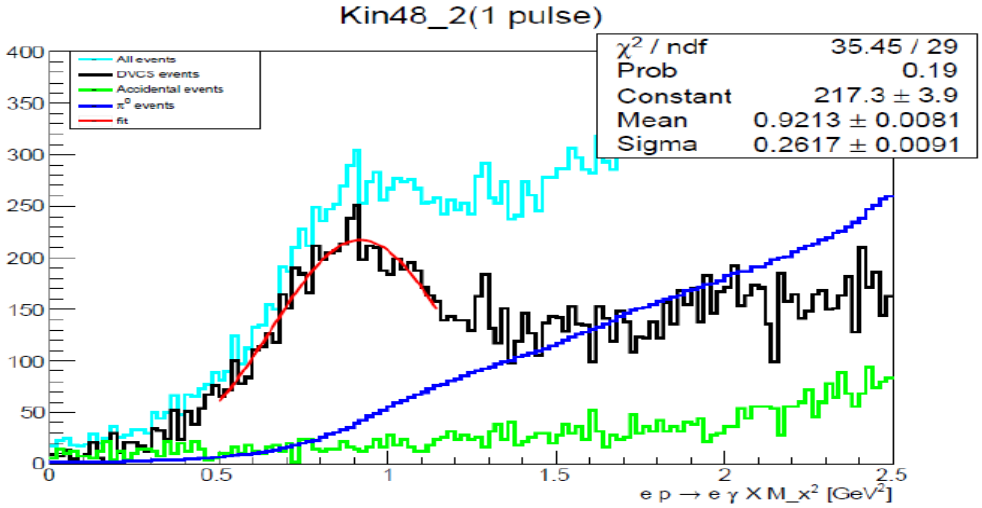

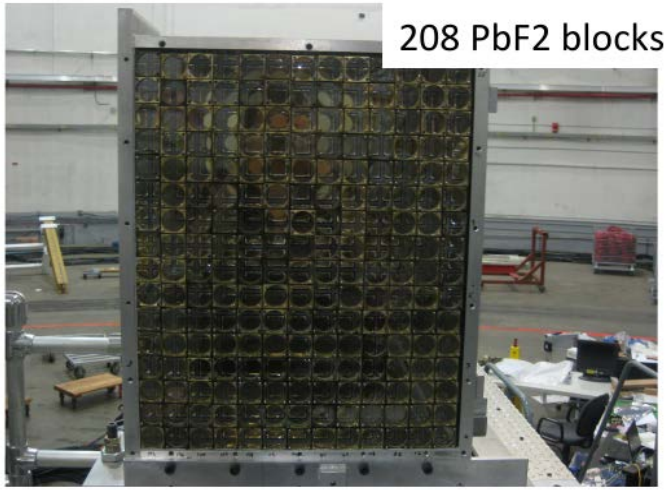

So far...

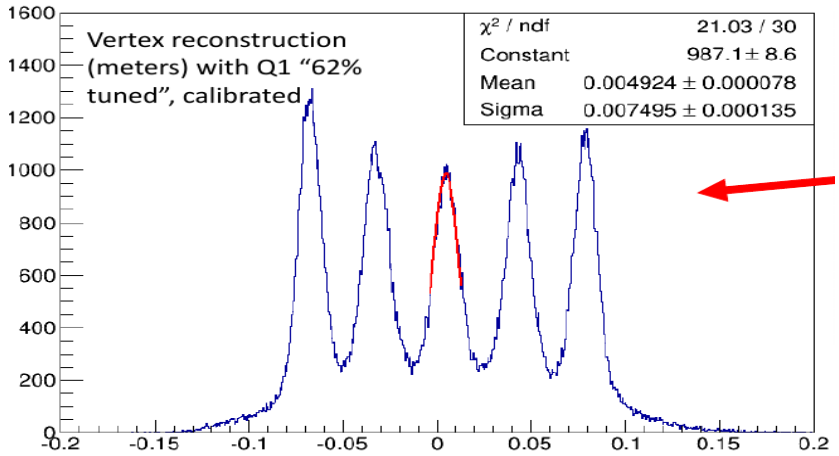

Optics calibration
Vertex reconstruction

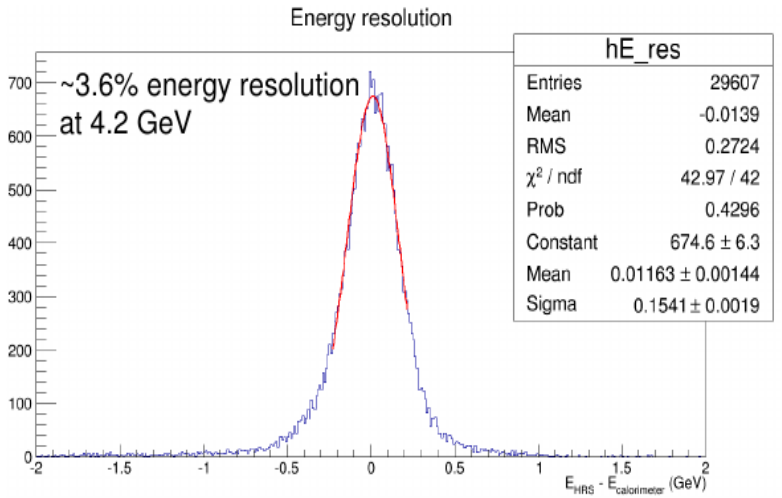

Calorimeter Calibration

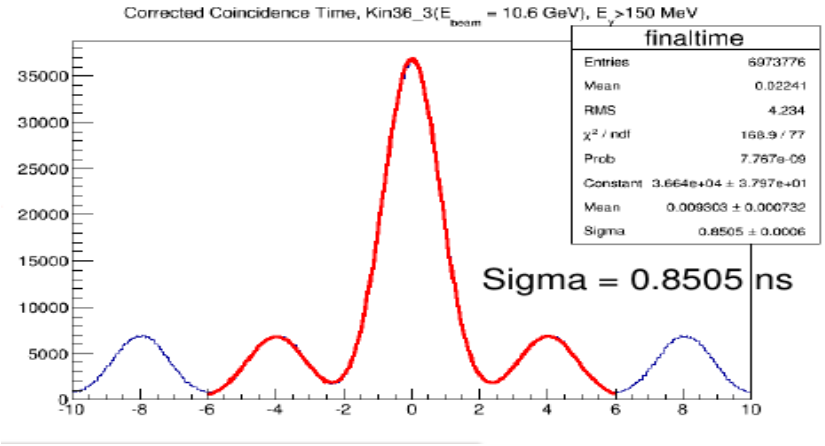

Coincidence time correction

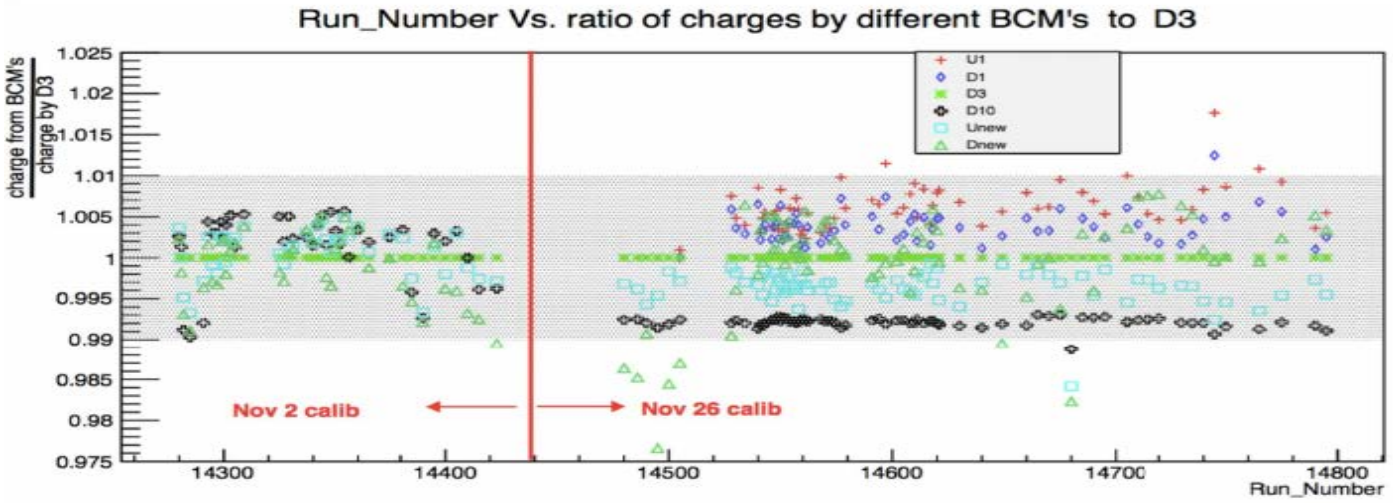

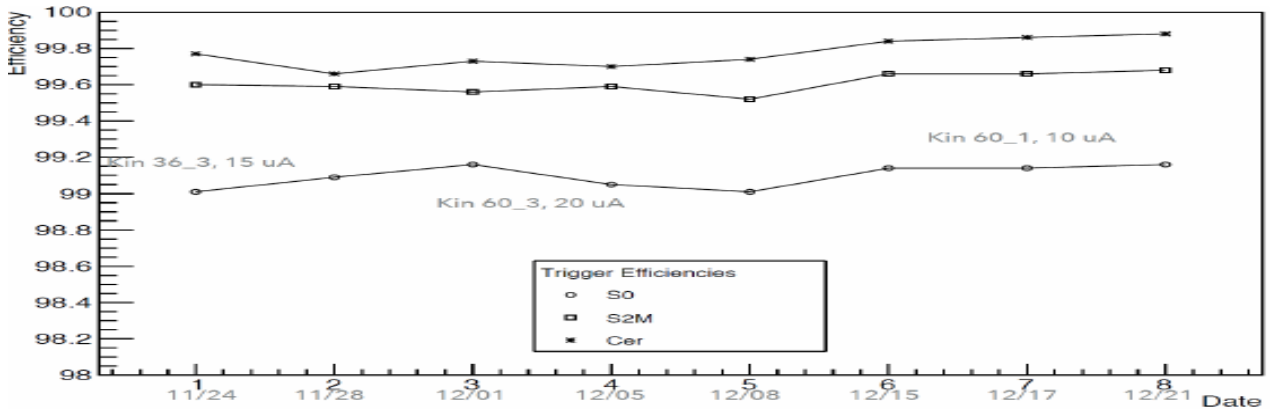

So far ...

Charge Measurement:
BCMs calibrated measured charge agrees within 1% from different BCMs

Efficiency of triggers:
S0, S2 and Cherenkov > 99%

Conclusion and Outlook:

- Data taking completed at end of 2016.
  - ✔ In each X_B several Q^2 Scans.
- Data analysis already started.
- Exciting results to come.

Acknowledgments:

Hall A DVCS Collaboration
Hall A Collaboration
Hall A technical staff
Accelerator staff

Thank you !!!

References

[1] X.-D. Ji, Phys. Rev. Lett. **78**, 610 (1997).

[2] D. Müller, D. Robaschik, B. Geyer, F. M. Dittes, and J. Hoeji, Fortsch. Phys. **42**, 101 (1994).

[3] A. V. Radyushkin *et al.*, Phys. Rev. **D56**, 5524 (1997).

[4] F. D. Aaron *et al.* (H1), Phys. Lett. **B681**, 391 (2009), arXiv:0907.5289 [hep-ex] .

[5] A. Airapetian *et al.* (HERMES), JHEP **07**, 032 (2012).

[6] E. Seder *et al.* (CLAS), Phys. Rev. Lett. **114**, 032001 (2015).

[7] C. M. Camacho *et al.*, Phys. Rev. Lett. **97**, 262002 (2006), arXiv:nucl-ex/0607029 [nucl-ex] .

[8] J. Roche *et al.*, (2006), arXiv:nucl-ex/0609015 [nucl-ex] .

[9] J. C. Collins and A. Freund, Phys. Rev. **D59**, 074009 (1999).

[10] M. Mazouz, de l'Universite Joseph Fourier **PhD Thesis** (2006).

[11] M. Guidal, H. Moutarde, and M. Vanderhaeghen, Rept. Prog. Phys. **76**, 066202 (2013).

[12] X. Ji, Ann. Rev. Nucl. Part. Sci. **54**, 413 (2004).

[13] A. V. Belitsky, D. Mueller, and A. Kirchner, Nucl. Phys. **B629**, 323 (2002).

[14] A. Bacchetta, U. D'Alesio, M. Diehl, and C. A. Miller, Phys. Rev. D **70**, 117504 (2004).

[15] S. Chen, The Florida State University **PhD Thesis** (2006).

[16] K. Kumeriki and D. Müller, EPJ Web Conf. **112**, 01012 (2016).

[17] A. Aktas *et al.* (H1), Eur. Phys. J. **C44**, 1 (2005).

[18] S. Chekanov *et al.* (ZEUS), Phys. Lett. **B573**, 46 (2003).

[19] H. S. Jo *et al.* (CLAS Collaboration), Phys. Rev. Lett. **115**, 212003 (2015).

[20] M. Defurne *et al.*, (2017), arXiv:1703.09442 [hep-ex] .

[21] A. Accardi *et al.*, Eur. Phys. J. **A52**, 268 (2016).

[22] K. Kumericki, S. Liuti, and H. Moutarde, "bibfield journal "bibinfo journal Eur. Phys. J." "textbf "bibinfo volume A52," "bibinfo pages 157 ("bibinfo year 2016), arXiv:1602.02763 [hep-ph] .

[23] H. Moutarde *et al.*, Phys. Rev. **D79**, 094021 (2009).

[24] M. V. Polyakov and A. G. Shuvaev, (2002), arXiv:hep-ph/0207153 [hep-ph] .

[25] K. Goeke, M. V. Polyakov, and M. Vanderhaeghen, Prog. Part. Nucl. Phys. **47**, 401 (2001), arXiv:hep-ph/0106012 [hep-ph] .

[26] C. Camacho, de l' Universite Paris VI **PhD Thesis** (2005).

[27] J. Alcorn *et al.*, Nucl. Instrum. Meth. **A522**, 294 (2004).

[28] O. Glamazdin et al., "Beam polarization: Raw results," `http://hallaweb.jlab.org/equipment/moller/raw_results.html`.

[29] W. Barry *et al.*, **JLab-TN-91-087**.

[30] D. W. Higinbotham et al., "Determination of the Beam Energy," `https://www.jlab.org/indico/event/197/session/3/contribution/12/material/slides/0.pdf`.

[31] K.Unser, Nucl. Sci **NS 28**, 2344 (1981).

[32] M. Defurne, Universite Paris-SUD **PhD Thesis** (2015).

[33] F. Feinstein (ANTARES), *New developments in photodetection. Proceedings, 3rd 2002*, Nucl. Instrum. Meth. **A504**, 258 (2003).

[34] J. Denard *et al.*, "High Accuracy Beam Current Monitor System For CEBAF's Experimental Hall A ," `https://accelconf.web.cern.ch/accelconf/p01/PAPERS/WPAH103.PDF`.